Journal of Environmental Chemical Engineering 14 (2026) 125606

Contents lists available at ScienceDirect

Journal of Environmental Chemical Engineering

journal homepage: www.elsevier.com/locate/jece

Rationally engineered Mg-based microspheres for efficient co-uptake of As(V) and fluoride: Adsorption performance and mechanistic insights

Zhao Hu [b], Xianfei Wang [a], Jingjing Fu [a], Jiantao Xu [a], Feihu Li [a,c,*]

[a] Aquatic Chemistry & Ecomaterials Laboratory (ACE Lab), School of Environmental Science and Engineering, Nanjing University of Information Science and Technology, 219 Ningliu Road, Nanjing, 210044, China
[b] Changwang School of Honors, Nanjing University of Information Science and Technology, 219 Ningliu Road, Nanjing, 210044, China
[c] NUIST Reading Academy, Nanjing University of Information Science and Technology, 219 Ningliu Road, Nanjing, 210044, China

ARTICLE INFO

Keywords:
Mg-based microspheres
Arsenate
Fluoride
Co-adsorption
Competitive adsorption
Surface complexation

ABSTRACT

Arsenate [As(V)] and fluoride (F^-) frequently coexist in contaminated waters, yet their simultaneous removal remains challenging because of competitive interactions and differences in interfacial affinity. Herein, MgO, Mg–Si, and Mg–Si–Zr microspheres were developed via a facile aerosol-spray-assisted approach to elucidate how Si and Zr incorporation regulate the co-uptake of As(V) and F^-. The adsorbents exhibited greatly different structural and surface characteristics, while all maintained high anion removal over pH 5.0–11.0. Adsorption was largely insensitive to ionic strength, particularly for As(V), indicating the predominance of specific surface interactions over sole electrostatic association. Increasing surface loading progressively decreased percentage removal, confirming finite and heterogeneous adsorption sites. Langmuir modeling generally described the equilibrium data well, with Mg–Si–Zr exhibiting the highest As(V) capacity (81.68 mg g^{-1} at 303 K), whereas MgO showed the highest F^- capacity (89.31 mg g^{-1}). Binary adsorption caused only moderate capacity losses, and Mg–Si–Zr retained 76.07 mg g^{-1} As(V) and 60.11 mg g^{-1} F^- at 303 K. Notably, molecule-level spectroscopic analyses revealed surface hydroxyl perturbation, formation of As–O species, metal-associated fluoride, and altered Mg/Zr coordination environments. These results demonstrate that Si and Zr incorporation creates complementary adsorption interfacial environments that enable efficient As(V)/F^- co-removal through specific surface complexation and ligand exchange with partial competition and electrostatic attraction. These findings indicate that the rationally engineered Mg–Si–Zr microspheres are a promising candidate for remediation of As/F coexisting wastewater, and provide a mechanistic basis for designing multifunctional Mg-based adsorbents for waters containing multiple anionic contaminants.

1. Introduction

Arsenic and fluoride are ubiquitous geogenic contaminants of groundwater and may occur simultaneously under alkaline and hydrogeochemically evolved conditions, particularly in arid and semi-arid aquifers [1,2]. Their co-occurrence is of particular concern because chronic exposure to elevated concentrations of either contaminant can cause severe adverse health effects, while their simultaneous occurrence complicates risk assessment and water treatment [3]. Recent hydrogeochemical investigations have confirmed the coexistence of elevated As and F^- in groundwater systems in Asia and elsewhere, demonstrating that their enrichment can be controlled by coupled processes including mineral dissolution, ion exchange, reductive desorption, and groundwater evolution [4,5]. Conventional treatment strategies, however, are often optimized for a single contaminant and may exhibit diminished performance when multiple oxyanions compete for the same reactive surface sites [6]. Thus, developing adsorbents capable of simultaneously capturing As(V) and F^- while maintaining high affinity under variable aqueous chemistry is important for practical treatment of multi-contaminant waters.

Adsorption is particularly attractive for As(V) and F^- removal because of its operational simplicity, relatively low energy demand, and potential for application to dilute contaminated waters [7–11]. Nevertheless, simultaneous adsorption of these two anions is more complex

* Corresponding author at: Aquatic Chemistry & Ecomaterials Laboratory (ACE Lab), School of Environmental Science and Engineering, Nanjing University of Information Science and Technology, 219 Ningliu Road, Nanjing 210044, China.
E-mail address: fhli@nuist.edu.cn (F. Li).

https://doi.org/10.1016/j.jece.2026.125606
Received 19 August 2026; Received in revised form 10 October 2026; Accepted 21 October 2026
Available online 22 October 2026
2213-3437/© 2026 Elsevier Ltd. All rights are reserved, including those for text and data mining, AI training, and similar technologies.

than their unary uptake because As(V) and F^- can compete for surface hydroxyls and metal-centered binding sites, while their adsorption affinities are strongly influenced by pH, ionic strength, surface loading, and adsorbent composition [12]. Recent studies have increasingly addressed this problem under binary rather than single-solute conditions, demonstrating that the presence of one oxyanion can substantially modify the adsorption capacity and selectivity toward the other [13–15]. For instance, recent modeling of single and competitive As(V)/F^- adsorption demonstrated distinct competitive responses and highlighted the importance of adsorbent characteristics and process configuration in determining competitive behavior [13,14]. Recent multifunctional metal-oxide systems have further demonstrated that chemically differentiated sites can promote simultaneous uptake of As and F; for example, porous Al/Ce oxides were reported to achieve rapid co-removal through distinct Al/Ce-associated interactions [16]. A recent Fe–Al-MOF/carbon-felt system further extended this concept to continuous-flow treatment, achieving simultaneous As/F removal with stable performance [17]. Accordingly, elucidating how surface composition regulates site availability, adsorption capacity, and competition between As(V) and F^- is essential for rational adsorbent design.

Mg-based materials are promising candidates for this purpose because MgO and related Mg-containing phases possess abundant basic surface sites and strong affinity toward fluoride and other oxyanions [10,18–20]. For instance, a recent study has directly demonstrated the feasibility of simultaneous As(V) and F^- removal using MgO, $Mg(OH)_2$, and $MgCO_3$, with MgO showing the strongest overall performance and preferential As(V) removal under the investigated conditions [10]. Recent studies have also reported effective fluoride removal by MgO, with adsorption associated with surface hydroxyl interactions and Mg-centered surface chemistry [21]. MgO offers a particularly relevant starting platform for As(V)/F^- co-removal due to its strong anion affinity toward both anions [10]. However, pristine MgO can suffer from structural instability under acidic conditions, and its adsorption selectivity toward different oxyanions is strongly dependent on surface structure and chemistry [22]. Incorporating secondary elements into MgO therefore provides an attractive route to tailor surface functionality and create complementary adsorption sites. In particular, Si incorporation can modify the crystallinity, porosity, and surface hydroxyl environment of MgO, whereas Zr-containing oxides are well known for their strong affinity toward oxyanions through specific surface complexation [23–25]. Recent studies have demonstrated that hydrated Zr oxides can form strong inner-sphere complexes with arsenate, highlighting the potential of Zr incorporation to introduce high-affinity sites for As(V) [23,24]. Despite these advances, it remains unclear how deliberate compositional engineering of Mg-based adsorbents can affect their surface structure and thereby regulate the balance among intrinsic As(V)/F^- affinity, competitive inhibition, and co-adsorption selectivity. In particular, the combined effects of Si-induced structural modification and Zr-associated high-affinity surface environments on As(V)/F^- co-uptake have not been systematically established.

Herein, MgO, Mg–Si, and Mg–Si–Zr microspheres were rationally constructed following a stepwise material-design strategy to establish the relationship between surface composition and the co-uptake of As(V) and F^-. MgO serves as the parent Mg-based adsorbent, Mg–Si represents the Si-modified intermediate, and Mg–Si–Zr represents the final multicomponent material incorporating Zr-containing surface domains. A Mg–Zr analogue would be a valuable complementary control, but it is beyond the compositional scope of the present study. The physicochemical characteristics of the microspheres were first correlated with their pH- and ionic-strength-dependent adsorption behavior to distinguish the contributions of electrostatic interactions and specific surface complexation. The effects of surface loading were subsequently examined to elucidate site saturation and surface heterogeneity, followed by quantitative comparison of unary and binary adsorption isotherms at different temperatures to resolve capacity changes, competition, and selectivity. Finally, molecular-scale spectroscopic analyses were combined to identify changes in surface hydroxyl, metal–oxygen, and adsorbate-related environments and thereby establish a molecular-level picture of the co-adsorption process. This integrated approach provides a mechanistic basis for understanding how Si and Zr incorporation creates complementary adsorption environments in Mg-based microspheres and offers design principles for simultaneous removal of As(V) and F^- from multi-contaminant aqueous systems. The novelty of the current work lies in systematically engineering a Mg-based microsphere from MgO, Mg–Si, to Mg–Si–Zr and resolving how structural/textural modification and Zr-associated surface chemistry regulate As(V)/F^- adsorption, competitive inhibition, and co-adsorption mechanisms.

2. Materials and methods

2.1. Materials

Pluronic F127 was purchased from Sigma-Aldrich (Shanghai, China), magnesium nitrate hexahydrate ($Mg(NO_3)_2{\cdot}6\,H_2O$, $\geq$ 99%), acetic acid ($C_2H_4O_2$, $\geq$99.5%), hydrochloric acid (HCl, 36.0–38.0%), ethanol (C_2H_6O, $\geq$99.5%), tetraethyl orthosilicate (TEOS), sodium fluoride (NaF, $\geq$98.0%), and zirconium nitrate pentahydrate ($Zr(NO_3)_4{\cdot}5\,H_2O$, $\geq$ 99.5%) were obtained from Sinopharm Chemical Reagent Co., Ltd (Shanghai, China) and used as received. Ultrapure deionized water (18 MΩ·cm at 25 °C) was used to prepare solutions. The As(V) and F^- stock solutions (1.0 M) were prepared by dissolving a certain amount of $Na_2HAsO_4{\cdot}7\,H_2O$ ($\geq$98.0, JT Baker Chemical, USA) and NaF into 100 mL of ultrapure water, respectively, and stored in a refrigerator at 4 °C for further use.

2.2. Preparation and characterization of Mg-based microspheres

An aerosol-spray-assisted approach (ASAA) was employed to synthesize the Mg-based microspheres due to its precise controllability and operational simplicity [26]. The synthesis protocol was modified from the ASAA and the acetic acid–hydrochloric acid–ethanol (AcHE) sol–gel system reported previously [27,28]. Briefly, magnesium nitrate, acetic acid, hydrochloric acid, ethanol, and Pluronic F127 were mixed at a molar ratio of 1:4:1.2:10:0.01 and stirred for 3 h to obtain a homogeneous precursor solution. For MgO synthesis, the precursor solution was directly transferred to a spray atomizer and introduced into a box-type resistance furnace preheated to 100 °C, followed by calcination at 350 °C for 5 h. For Mg–Si synthesis, tetraethyl orthosilicate (TEOS) was added to the precursor solution to achieve a Mg:Si molar ratio of 1:1 before atomization and calcination under identical conditions. For Mg–Si–Zr synthesis, TEOS and zirconium nitrate pentahydrate were further incorporated into the precursor solution to obtain a Mg:Si:Zr molar ratio of 1:1:1. After homogeneous mixing, the solution was atomized and calcined following the same procedure to produce the Mg–Si–Zr microspheres (Fig. 1a). Note that the nominal Mg:Si and Mg:Si:Zr precursor molar ratios were set at 1:1 and 1:1:1, respectively, to obtain representative binary and ternary formulations for comparison with the MgO reference material. The selected ratios were intended to support a stepwise investigation of compositional modification rather than to identify an optimal composition. No systematic screening of alternative Si or Zr contents was conducted; therefore, the selected precursor ratios do not establish the optimum composition or the actual elemental ratios of the resulting materials.

X-ray diffraction analysis was performed on an XRD-6100 diffractometer (Shimadzu, Japan) at a tube voltage of 40 kV and a tube current of 30 mA with Cu-Kα radiation (step size: 0.02°, scanning rate: 7° min^{-1}). Scanning electron microscopy (SEM) was performed using a Hitachi SU1510 microscope at an accelerating voltage of 15.0 kV. The Brunauer-Emmett-Teller (BET) surface areas were obtained by the N_2 adsorption method using a Quantachrome gas adsorption analyzer (iQ-AG-MP). Fourier Transform Infrared Spectroscopy (FTIR) data were recorded in the wavenumber range of 4000–400 cm^{-1} on an Is5 infrared

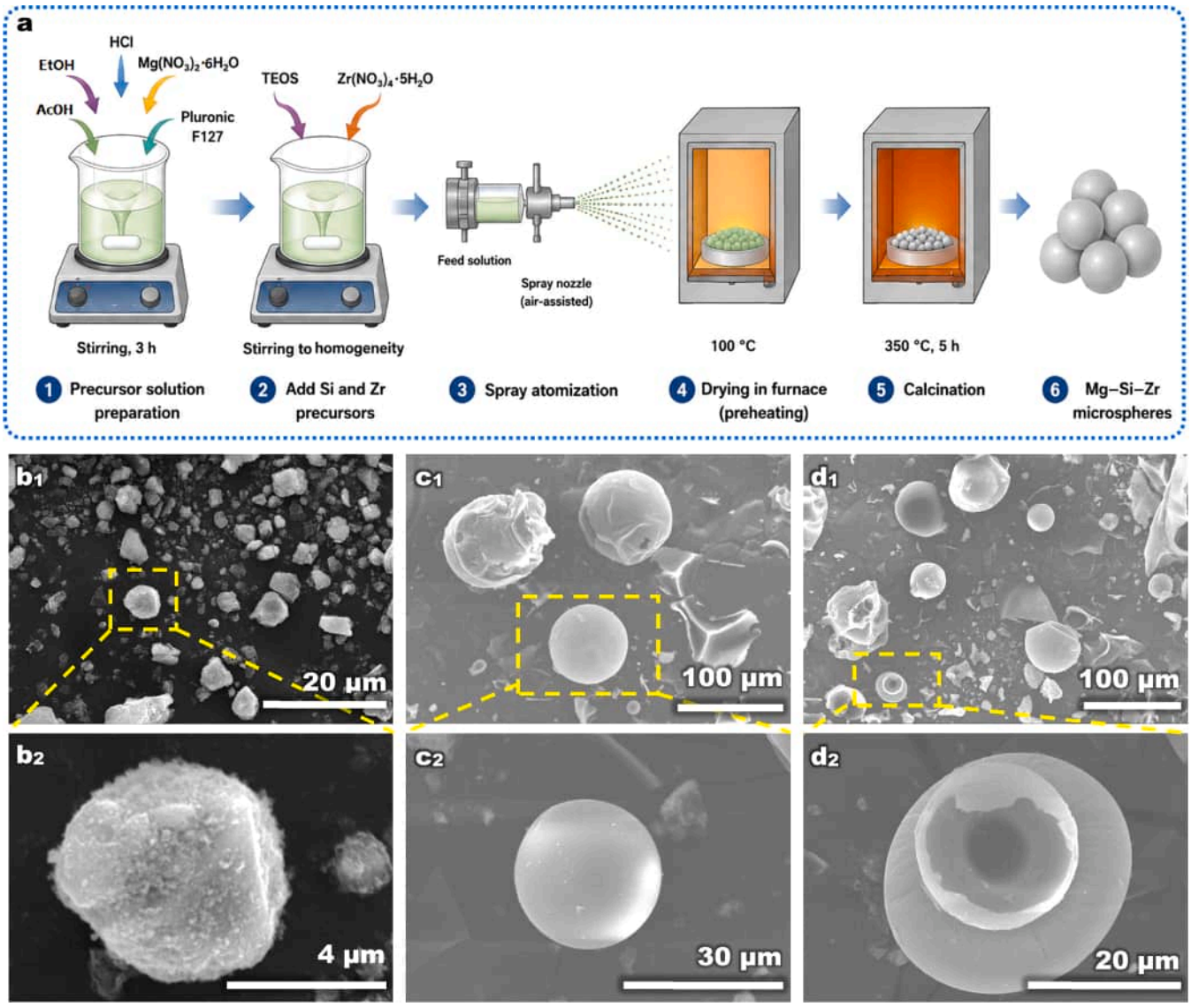


Fig. 1. (**a**) Schematic illustration of the preparation step of the Mg-Si-Zr microspheres, (**b**–**d**) SEM images of the as-prepared Mg-based microspheres at varying magnifications: (**b**$_1$, **b**$_2$) MgO, (**c**$_1$, **c**$_2$) Mg-Si, and (**d**$_1$, **d**$_2$) Mg-Si-Zr microspheres.

spectrometer (Thermo Nicolet, USA) using spectroscopic-grade dried KBr as the matrix material. Before the FTIR measurements, all the samples along with KBr were oven-dried overnight at 60 °C. X-ray photoelectron spectroscopy (XPS) analysis was conducted on a PHI 5000 spectroscope (Versa Probe, UIVAC-PHI, Japan) equipped with a monochromatized Al Kα X-ray source ($h\nu$ = 1486.6 eV). The C 1 s peak at 284.8 eV was used for calibration of the binding energy values of other elements of concern.

2.3. Adsorption tests

The three as-prepared Mg-based microspheres were then evaluated as adsorbents for co-adsorption of As(V) and F^- by batch experiments. Unless otherwise specified, all batch adsorption experiments were conducted in triplicate at atmospheric pressure and room temperature (298 ± 1 K). Adsorption suspensions were prepared in 15 mL polyethylene centrifuge tubes by mixing the adsorbent with appropriate volumes of As(V) and/or F^- stock solutions and $NaNO_3$ background electrolyte to obtain a total solution volume of 10 mL. Note that our current experiments were conducted under controlled $NaNO_3$ electrolyte conditions to isolate the intrinsic As(V)/F^- co-adsorption behavior. The effects of naturally occurring competing anions and complex groundwater matrices were not systematically evaluated and warrant further investigation before field-scale application. The ionic strength was adjusted to 1, 10, or 100 mM using $NaNO_3$, and the adsorbent dosage was maintained at 0.5 g L^{-1} unless otherwise stated. The solution pH was adjusted to 4.0–11.0 using 0.5 or 1.0 M HNO_3 and NaOH. After purging with N_2 for 5 min to remove dissolved CO_2, the suspensions were sealed quickly and then flipped on a rotator (Thermo Scientific, USA) at 60 rpm. A contact time of 24 h was selected to ensure equilibrium based on our previous studies of As(V)/F^- co-adsorption using metal-oxide-based adsorbents [9,12,29]. Subsequently, the suspensions were centrifuged at 12,000 rpm for 15 min, and the supernatants were filtered through 0.45 μm polyethersulfone (PES) membranes (Navigator, Tianjin, China). Following an earlier procedure [9], equilibrium concentrations of As(V) and F^- were determined using an atomic fluorescence spectrometer (AFS-200T, Skyray Instrument, China) and a visible spectrophotometer (JH723PC, Jinghua Instrument, China), respectively. Specifically, As(V) concentrations were quantified by hydride-generation atomic fluorescence spectrometry (HG-AFS) using a hollow-cathode lamp at 193.7 nm [30,31]. F^- concentrations were determined colorimetrically at 620 nm

using Alizarin complexone as the color-developing reagent [32]. Solution pH was measured using a calibrated pH meter (Orion Model 868, Thermo Scientific, USA). The adsorption capacity (q_e, mg g^{-1}) and removal efficiency (%R) were calculated according to Eqs. (1) and (2),

$$q_e = \frac{(C_0 - C_e)V}{m} \quad (1)$$

$$\%R = \frac{C_0 - C_e}{C_0} \times 100\% \quad (2)$$

where C_0 and C_e are the initial and equilibrium concentrations of the target adsorbate in solution (in mg L^{-1}), respectively, and V refers to the volume of the solution (L).

Adsorption isotherms were obtained at pH 7.0. For single-solute systems, the initial As(V) and F^- concentrations ranged from 1 to 100 mg As L^{-1} and 1–50 mg F L^{-1} , respectively. For binary-solute systems, the initial concentrations of As(V) and F^- were simultaneously varied over the same concentration ranges. Both the unary and binary adsorption isotherm experiments were conducted at 283 and 303 K using the same dosage of 0.5 g L^{-1} . The equilibrium adsorption data were fitted using the Langmuir and Freundlich isotherm models that are formulated below,

Freundlich model:

$$q_e = k_F C_e^{1/n} \quad (3)$$

Langmuir model:

$$q_e = \frac{k_L q_m C_e}{1 + k_L C_e} \quad (4)$$

where k_F (mg^{1-n} L^n g^{-1}) and n denote the Freundlich constants, k_L refers to the Langmuir adsorption energy constant (L mg^{-1}), and q_m stands for the theoretical maximum adsorption capacity.

3. Results and discussion

3.1. Properties of the as-prepared Mg-based microspheres and target adsorbates

As specified above, the Mg-based microspheres were prepared through the ASAA route. Compared with conventional synthesis routes, the ASAA offers several advantages for the fabrication of multicomponent microspheres. Solution precipitation is simple and economical but may provide less direct control over spherical morphology and particle aggregation, whereas sol–gel processing affords high compositional homogeneity and tunable textural properties but generally involves additional aging and drying steps. Hydrothermal/solvothermal synthesis provides effective control over crystallinity and morphology but commonly relies on pressurized batch reactors [33]. In ASAA processing, a homogeneous precursor solution is atomized into droplets, and rapid solvent evaporation converts the droplets directly into solid particles (Fig. 1a). This approach enables simultaneous control of particle morphology, size, porosity, and composition and is readily amenable to continuous and scalable production [27,28]. Accordingly, this method is particularly suitable for the present Mg–Si–Zr system, where spherical morphology and incorporation of multiple inorganic components are desired.

The SEM images reveal pronounced morphological evolution with the incorporation of Si and Zr (Fig. 1b–d and S1, Supplementary materials). Specifically, pristine MgO consists mainly of irregular, highly aggregated granular particles with rough and heterogeneous surfaces (Fig. 1b and S1a), indicating that the MgO precursor undergoes remarkable particle aggregation during thermal treatment. In contrast, introducing the Si precursor results in the formation of well-defined, intact spherical Mg-Si microspheres with relatively smooth surfaces (Fig. 1c and S1b). The formation of microspherical architectures is generally associated with the rapid solvent evaporation and confinement of precursor species within individual aerosol droplets during spray-assisted processing [27,28]. Further incorporation of Zr produces Mg-Si-Zr microspheres that largely preserve the spherical morphology but exhibit obviously different surface architectures, characterized by surface fracturing, crumpled layers, and apparent hollow or core–shell-like structures (Fig. 1d and S1c). The exposed cavities and fractured surfaces suggest that the ternary microspheres possess a more open architecture than the relatively compact Mg-Si spheres (see Fig. 1c), potentially facilitating access to internal surfaces. Such morphological evolution is important because the accessible external and internal surfaces ultimately determine the solid–water interfacial area available for interaction with aqueous oxyanions [12,29]. Collectively, the SEM observations demonstrate that Si and subsequent Zr incorporation do not merely alter the chemical composition of the MgO matrix but also substantially reconstruct its microscale architecture, providing three physically distinct Mg-based adsorption interfaces for the subsequent comparison of As(V) and F^- uptake.

The structural and surface-chemical characteristics of these microspheres were further examined by XRD and FTIR, while their textural properties were evaluated from N_2 adsorption–desorption measurements (Fig. 2). Specifically, pristine MgO exhibits several sharp and well-resolved diffraction peaks that are consistent with the standard MgO phase (JCPDS #78–0430) [34], confirming its highly crystalline structure (Fig. 2a). In contrast, Mg–Si and Mg–Si–Zr showed only broad diffuse humps without distinct crystalline peaks, indicating predominantly amorphous or poorly crystalline structures. This difference can be attributed to the incorporation of Si and Zr into the Mg–O framework. Si-containing structural units substantially disrupt the long-range ordering of MgO and promote the formation of a chemically heterogeneous oxygen-coordinated network, while subsequent Zr incorporation further increases structural disorder and inhibits the development of well-defined crystalline domains [35]. The FTIR spectra provide complementary evidence for changes in the chemical environment of the microspheres (Fig. 2b). All three materials show a broad band centered at approximately 3440 cm^{-1} and a band near 1638 cm^{-1} , which can be attributed to O–H stretching and H–O–H bending vibrations (δ_{H2O}) associated with surface hydroxyl groups and/or adsorbed water, respectively [36]. A band around 460 cm^{-1} is assigned to Mg–O vibrations [7], whereas a pronounced band near 1010 cm^{-1} emerges after Si incorporation and remains evident in Mg-Si-Zr. This band is associated with Si–O-, Zr–O-, and/or interconnected Si–O–Mg/Zr vibrations, supporting the formation of Si/Zr-containing oxygen-coordination environments within the modified Mg-based matrix [9,37]. These crystallographic and spectroscopic results therefore collectively demonstrate a transition from crystalline MgO toward structurally disordered Si- and Zr-doped oxygen-coordinated matrices, accompanied by extensive changes in their intrinsic oxide-like chemical environments. Therefore, Mg–Si–Zr microspheres are predominantly composed of oxygen-coordinated Mg-, Si-, and Zr-containing species rather than metallic phases. Besides, this observation supports the incorporation of Si- and Zr-associated structural units into the materials but does not establish their spatial distribution or the exact bulk elemental composition. Accordingly, Mg–Si and Mg–Si–Zr are used as synthesis-based sample designations rather than stoichiometric formulas. Consistent with the above observations, the N_2 adsorption–desorption isotherms are Type IV isotherms along with pronounced H_1-type hysteresis for all three materials (Fig. 2c), indicative of mesoporous structures [38]. The BET surface area increased markedly from 50 m^2 g^{-1} for MgO to 200 m^2 g^{-1} for Mg–Si, which can be attributed to the substantial textural reorganization induced by Si incorporation. The highly crystalline and aggregated MgO structure was transformed into a more disordered Mg–O–Si matrix, accompanied by the development of a narrower mesoporous distribution centered at ~7.8 nm (Fig. 2d). This combination of reduced long-range crystallinity, suppressed aggregation, and increased mesopore development likely generated substantially greater accessible

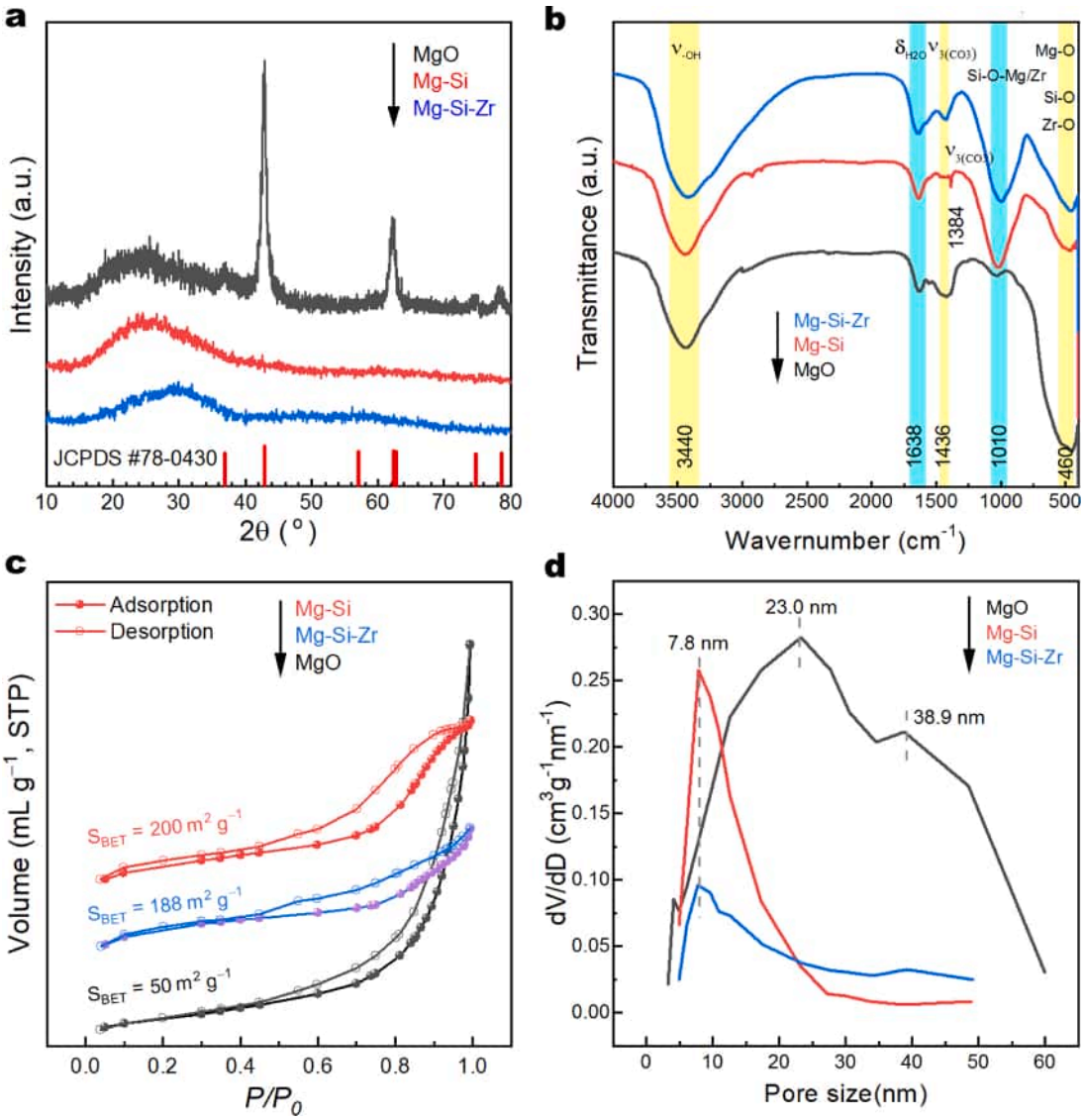


Fig. 2. Characterization of Mg-based microspheres: (**a**) XRD patterns (JCPDS #78–0430 is the standard XRD card of MgO), (**b**) FTIR spectra, (**c**) N_2 adsorption-desorption isotherms, and (**d**) pore size distribution profiles.

surface area. Further incorporation of Zr slightly decreased the BET surface area to 188 $m^2\ g^{-1}$. The corresponding broadening of the pore-size distribution to approximately 8–10 nm suggests that Zr incorporation modified the pore network and may have reduced the accessibility of a fraction of the mesoporous surface, possibly through local framework densification and/or partial pore blocking [31]. Nevertheless, Mg–Si–Zr retained a substantially higher surface area than MgO. Thus, Si and Zr incorporation simultaneously modifies the phase structure, chemical bonding environment, and pore architecture of MgO, generating materials with substantially greater accessible surface areas and different distributions of mesoporous domains. These differences provide an essential physicochemical basis for subsequently disentangling the contributions of surface area, pore accessibility, and surface chemical environments to the co-uptake of As(V) and F^-.

Apart from the adsorbents, the aqueous speciation of the target adsorbates was also considered because the charge and protonation state of As(V) and F^- are strongly dependent on pH and therefore directly affect their interactions with the Mg-based interfaces (Fig. S2). Under ambient conditions, As(V) occurs as H_3AsO_4 at strongly acidic pH, with the first dissociation boundary (pKa_1) at pH 2.2. With increasing pH, $H_2AsO_4^-$ becomes the predominant species between pH 2.2 and 6.9, followed by $HAsO_4^{2-}$ between pH 6.9 and 11.5; at pH > 11.5, AsO_4^{3-} becomes dominant. The progressively increasing negative charge of As(V) with increasing pH is expected to alter both electrostatic interactions and ligand-exchange equilibria at proton-active mineral surfaces [39]. Fluoride exhibits a simpler speciation pattern, with neutral HF(aq) predominating below pH 3.2 and dissociated F^- becoming overwhelmingly dominant above this pH (Fig. S2b). Accordingly, over most of the pH range relevant to the adsorption experiments (4.0–11.0), both target contaminants are present predominantly as negatively charged species, although their charge states differ significantly, with As(V) evolving from monovalent to divalent and ultimately trivalent oxyanions as pH increases. This distinction is particularly relevant to the subsequent adsorption experiments because the pH-dependent protonation of surface hydroxyl groups on Mg-, Si-, and Zr-containing interfaces occurs concurrently with changes in aqueous As(V) and F^- speciation [7,9].

3.2. *Effects of pH and ionic strength on adsorption*

The adsorption envelopes of As(V) and F^- on MgO, Mg-Si, and Mg-Si-Zr microspheres are depicted as a function of pH and ionic strength (1,

10, and 100 mM $NaNO_3$) in Fig. 3. Despite differences in composition and surface structure, all three microspheres exhibited a broadly similar pH-dependent adsorption pattern for both adsorbates. Specifically, at pH 4.0, As(V) and F^- removal decreased markedly to approximately 30–55%, whereas adsorption rapidly increased with increasing pH and reached a relatively stable plateau over approximately pH 5.0–11.0. The pronounced decrease in As(V) and F^- removal at pH 4.0 is likely associated with acid-induced alteration of Mg-containing surface domains, potentially involving partial dissolution and restructuring of the Mg-based matrix. MgO is susceptible to proton-promoted surface restructuring and dissolution under acidic conditions, providing a plausible basis for this behavior [40]. However, because dissolved Mg^{2+} was not directly quantified in the present study, the contribution of acid-induced alteration of the Mg-containing matrix cannot be independently separated from other acid-induced changes in surface structure and chemistry. Once the solution pH increased above ~5.0, however, both As(V) and F^- removal recovered rapidly and remained relatively high over a broad pH window, indicating that the microspheres retained effective adsorption affinity under neutral and alkaline conditions. This behavior is particularly notable because increasing pH progressively increases the negative charge of As(V) (i.e., from $H_2AsO_4^-$ to $HAsO_4^{2-}$ and AsO_4^{3-}), while F^- remains the dominant fluoride species above pH 3.2 (Fig. S2). Thus, the sustained uptake over pH 5.0–11.0 cannot be explained simply by electrostatic attraction between positively charged surfaces and negatively charged adsorbates, even though MgO has an isoelectric point above 12.1 [7]. Rather, it points to the contribution of specific surface interactions that remain effective despite increasingly unfavorable electrostatic conditions and competition with OH^- at elevated pH [18,41,42]. Comparison among the three microspheres further reveals different adsorption preferences. For instance, MgO exhibited approximately 60–65% As(V) removal but considerably higher F^- removal of approximately 85–90% in the pH 6.0–10.0 region, indicating a stronger relative affinity toward fluoride. Incorporation of Si evidently increased As(V) removal to approximately 75–80% for Mg-Si, while maintaining F^- removal at approximately 80–85%. The enhanced As(V) uptake is consistent with the substantial structural and textural modification induced by Si incorporation, including the transition toward an amorphous matrix and the pronounced increase in BET surface area (Fig. 2c) [43,44]. Mg-Si-Zr maintained approximately 70–75% As(V) and 80–90% F^- removal, thereby combining high uptake of both contaminants. These results indicate that modification of MgO with Si and Zr changes not only the accessible interfacial area but also the chemical environment of the adsorption sites, allowing the relative affinity toward As(V) and F^- to be tailored. Besides, these data indicate that effective As(V)/F^- adsorption is maintained over approximately pH 5.0–11.0, suggesting that pH control above the strongly acidic region (pH $\geq$ 5.0) may be a practical first strategy. Overall, the pH-dependent adsorption behavior likely reflects the combined effects of aqueous As(V)/F^- speciation and changes in the protonation state of surface hydroxyl groups. Because the surface charge of the microspheres was not directly measured, the relative contribution of electrostatic interactions cannot be quantitatively resolved from the present data.

The dependence of adsorption on background ionic strength provides further insight into the nature of these interfacial interactions (Fig. 3). For As(V), the adsorption envelopes obtained at 1–100 mM $NaNO_3$ are closely clustered over the investigated pH range for MgO,

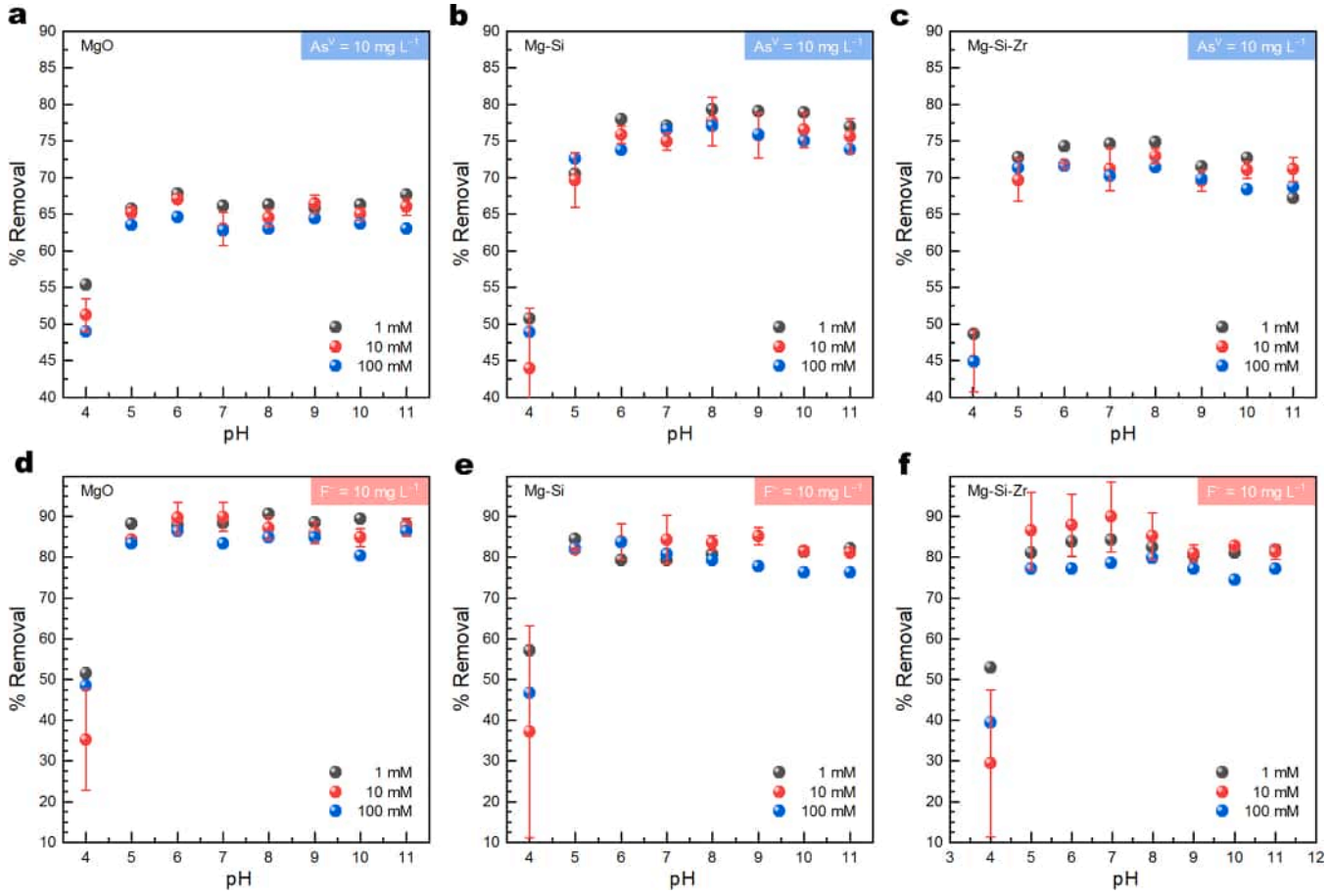


Fig. 3. Adsorption envelopes of (**a**) As(V) on MgO, (**b**) As(V) on Mg-Si, (**c**) As(V) on Mg-Si-Zr, (**d**) F^- on MgO, (**e**) F^- on Mg-Si, and (**f**) F^- on Mg-Si-Zr in individual solute solutions with 10 mg L^{-1} of As(V) or F^- at different pH and ionic strength (1–100 mM $NaNO_3$, dosage = 0.5 g L^{-1}, contact time = 24 h, temperature = 298 ± 1 K).

Mg-Si, and Mg-Si-Zr, with no pronounced shift in the adsorption profiles as ionic strength increased. Such weak ionic-strength dependence indicates that the uptake of As(V) is relatively insensitive to compression of the electrical double layer and/or competition from background electrolyte ions (i.e., NO_3^-) within the investigated range, suggesting that nonspecific electrostatic interactions are not the sole controlling factor [10,41]. Instead, the observations are consistent with a significant contribution from specific surface interactions, particularly inner-sphere surface complexation involving direct coordination of arsenate with surface metal centers and/or ligand exchange with surface hydroxyl groups [18,20,41]. In comparison, F^- adsorption remained high but exhibited a visible, albeit relatively modest, decrease at the highest ionic strength (100 mM $NaNO_3$) for all three microspheres. This weak ionic-strength dependence suggests that specific interactions likely dominate F^- retention as well, while a secondary contribution from electrostatic or outer-sphere interactions may become apparent at elevated electrolyte concentration [7]. Compression of the electrical double layer and/or competition between background electrolyte species and F^- for interfacial environments could account for the modest decrease in F^- uptake at 100 mM $NaNO_3$ [10]. The contrasting ionic-strength responses of As(V) and F^- therefore suggest that their adsorption is not controlled by an identical interfacial interaction: As(V) exhibits behavior more strongly indicative of specific, ionic-strength-insensitive interactions, whereas F^- retains a small but obvious electrostatic contribution. Importantly, the persistence of high adsorption over pH 5.0–11.0 and the generally weak response to ionic strength together suggest that specific surface interactions, rather than simple outer-sphere electrostatic attraction, contribute to the retention of both anions, with the relative contribution of nonspecific interactions being more apparent for F^-.

3.3. Effects of surface loading (C_0) on adsorption

The influence of surface loading on the uptake of As(V) and F^- was evaluated by varying the initial adsorbate concentration (C_0) from 2 to 30 mg L^{-1} at a constant ionic strength of 10 mM $NaNO_3$ (Fig. 4). For both adsorbates, all three microspheres exhibited very high fractional removal at the lowest loading of 2 mg L^{-1}, with removal generally exceeding 90% throughout the relatively stable pH range of 5.0–11.0. Obviously, the amount of adsorbate introduced into the suspension was low relative to the population of available surface sites; the most accessible and reactive sites could effectively capture the dissolved species. As C_0 increased to 10 and 30 mg L^{-1}, the removal efficiencies progressively decreased for both anions, whereas the overall shapes of the adsorption envelopes remained broadly comparable (Fig. 4). This concentration-dependent decrease in removal efficiency is indicative of progressive occupation of a finite population of adsorption sites: increasing the concentration rises the concentration gradient and mass-transfer driving force, but simultaneously increases the demand on the available surface sites, eventually causing a greater fraction of sites to become occupied [45]. Notably, a decrease in percentage removal does not necessarily indicate a decrease in the equilibrium adsorption capacity (q_e); at a fixed adsorbent dosage, a higher initial concentration can increase the absolute amount of adsorbate retained per unit mass even when the fraction removed from solution declines [46,47]. More importantly, the preservation of the overall pH-dependent profiles at

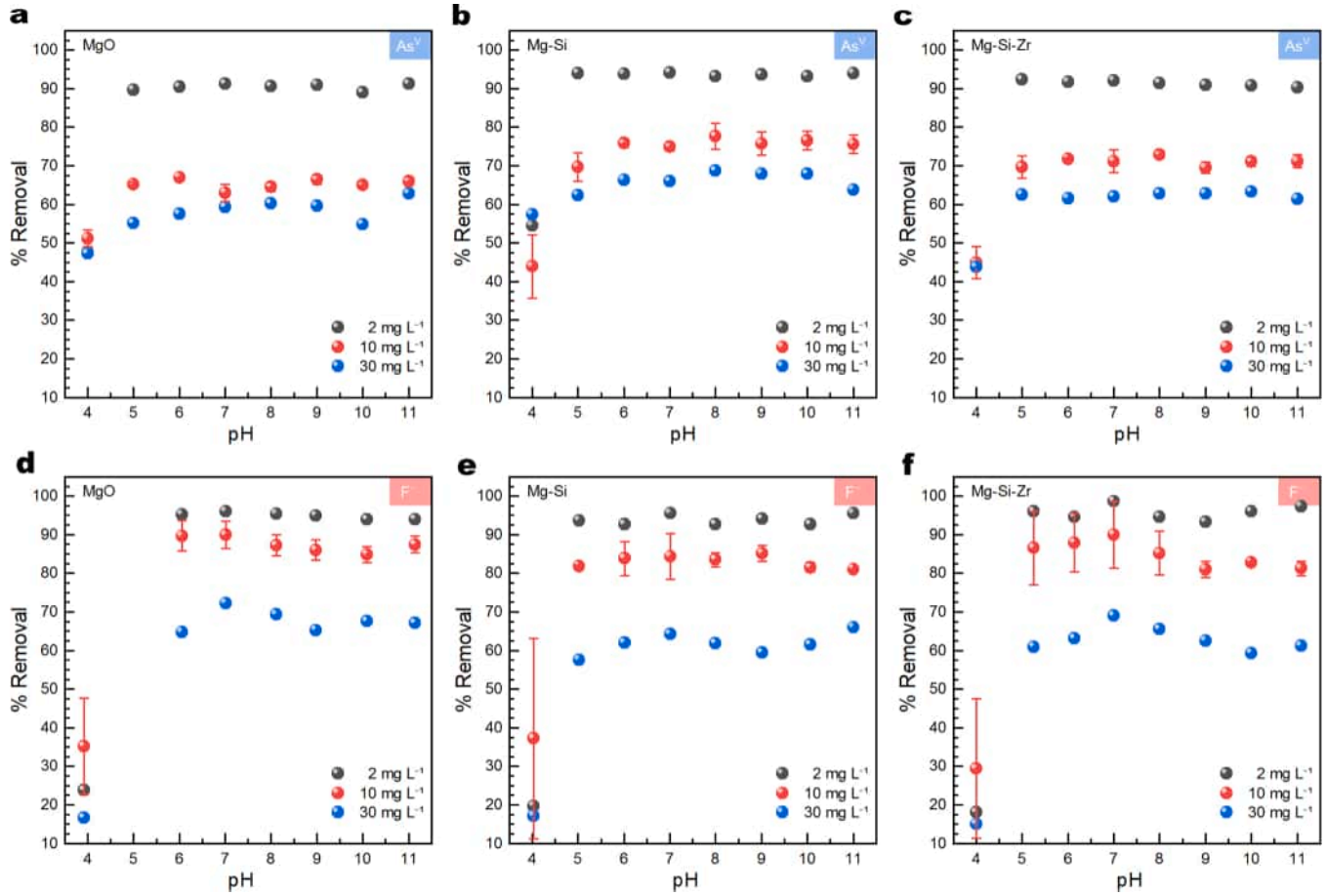


Fig. 4. Adsorption envelopes of (**a**) As(V) on MgO, (**b**) As(V) on Mg-Si, (**c**) As(V) on Mg-Si-Zr, (**d**) F^- on MgO, (**e**) F^- on Mg-Si, and (**f**) F^- on Mg-Si-Zr in individual solute solutions with a constant ionic strength (10 mM $NaNO_3$) and different surface loadings (2 −30 mg L^{-1} of As(V) or F^-, dosage = 0.5 g L^{-1}, contact time = 24 h, temperature = 298 ± 1 K).

different loadings provides evidence that the dominant physicochemical constraints governing adsorption remain operative as the surface becomes progressively occupied. In particular, an abrupt decrease in removal was consistently observed at pH 4.0 for all three adsorbents, both adsorbates, and the investigated loadings. This observation suggests that the acidic condition imposes a common limitation on adsorption, likely through acid-induced alteration of the Mg-containing surface/matrix. Because Mg^{2+} release was not directly quantified in this study, the specific contribution of Mg dissolution cannot be independently resolved. Above pH 5.0, however, the adsorption profiles at 10 and 30 mg L^{-1} largely followed the same broad pH-dependent trajectory observed at 2 mg L^{-1} , with substantial uptake maintained through pH 11.0. Therefore, increasing surface loading primarily reduced the removal efficiency rather than fundamentally changing the pH window over which the materials remained active. The persistence of high uptake under progressively greater adsorbate loading further suggests that these Mg-based microspheres contain a population of adsorption sites that remains chemically accessible across a broad pH range, although their relative contribution becomes increasingly important as the highest-affinity sites are progressively occupied.

The loading-dependent changes in the adsorption envelopes further provide indirect evidence for surface site heterogeneity. At low surface coverage, the abundance of vacant sites allows As(V) and F^- to preferentially interact with the most accessible and energetically favorable surface environments. With increasing loading, these high-affinity sites are progressively occupied, forcing subsequently introduced adsorbate molecules to utilize sites with comparatively lower affinity or different local coordination environments. Such sequential occupation of sites with different adsorption energies is a characteristic feature of heterogeneous surfaces and can manifest as loading-dependent changes in adsorption efficiency and the shape of adsorption profiles [46,48]. The three Mg-based microspheres displayed discernible differences under the highest loading of 30 mg L^{-1} , highlighting the role of their distinct structural and surface-chemical characteristics. For As(V), MgO showed the lowest removal, approximately 55–60%, whereas Mg-Si maintained a higher removal of approximately 65–70% over the relatively stable pH range. This enhanced resistance to site saturation is consistent with the substantially larger accessible surface area and modified amorphous surface structure of Mg-Si as verified above (Fig. 2), which can provide a larger and potentially more diverse population of accessible adsorption sites [43,44]. Mg-Si-Zr exhibited intermediate As(V) removal of approximately 60–70%, indicating that incorporation of Zr preserves substantial As(V) uptake while producing a surface chemically distinct from that of Mg-Si. For F^-, MgO and Mg-Si-Zr retained relatively strong performance even at 30 mg L^{-1} , with approximately 60–70% removal, demonstrating that the ternary material retains a high affinity toward fluoride under substantial surface loading. The favorable fluoride performance of Mg-Si-Zr may be associated with the introduction of Zr-containing surface groups, although the adsorption envelopes alone cannot distinguish the contributions of Zr-specific coordination from changes in surface area, pore accessibility, or the overall distribution of surface functional groups [49]. Importantly, the different loading responses of As(V) and F^- imply that both adsorbates do not necessarily utilize an identical population of surface sites. The results therefore suggest a progressive adsorption nature in which highly accessible/high-affinity sites dominate uptake at low coverage, followed

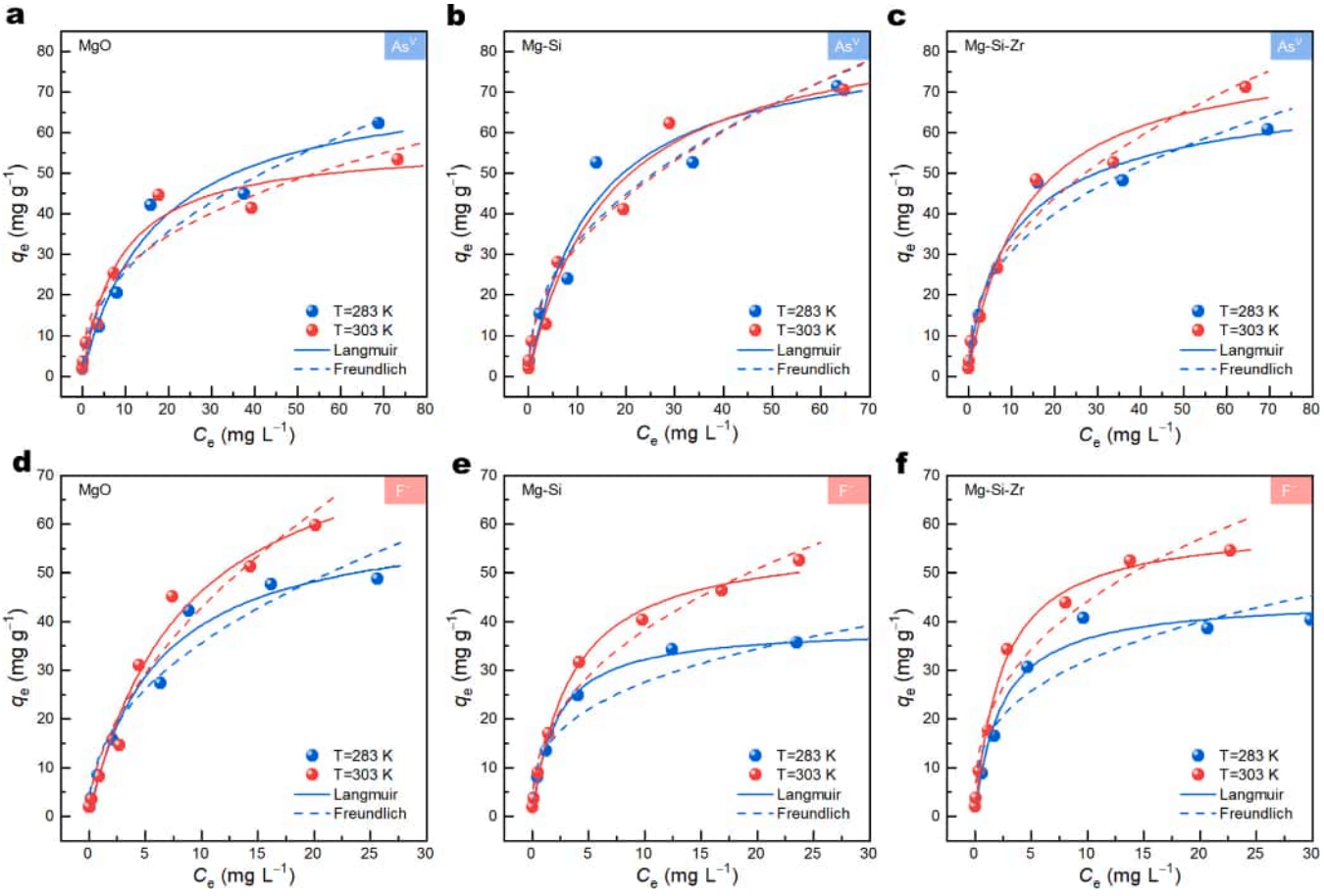


Fig. 5. Adsorption isotherms in unary matrices at 283 and 303 K: (**a**) As(V) on MgO, (**b**) As(V) on Mg-Si, (**c**) As(V) on Mg-Si-Zr, (**d**) F^- on MgO, (**e**) F^- on Mg-Si, and (**f**) F^- on Mg-Si-Zr (ionic strength = 10 mM $NaNO_3$, pH = 7.0, dosage = 0.5 g L^{-1}, contact time = 24 h). Solid and dashed lines represent Langmuir and Freundlich model fits, respectively.

progressively by less favorable or accessible sites as surface loading increases.

3.4. Adsorption isotherms

The unary adsorption isotherms of As(V) and F^- on these Mg-based microspheres at 283 and 303 K are presented in Fig. 5, with the corresponding binary systems shown in Fig. 6. For all adsorbent–adsorbate combinations, adsorption increased with equilibrium concentration (C_e) and gradually approached a plateau, indicating progressive occupation of available adsorption sites [12,47]. The experimental data were fitted using the nonlinear Langmuir and Freundlich models (Table 1). Obviously, the Langmuir model generally demonstrated the better fit, with higher R^2 values than the Freundlich model, indicating that the equilibrium data were better described by a finite-capacity adsorption model [50,51]. Nevertheless, the superior Langmuir fit should not be interpreted as proof that all surface sites are energetically identical, particularly given the heterogeneous structures of these Mg-based microspheres; rather, the Langmuir q_m values provide useful comparative measures of their apparent maximum adsorption capacities [52]. At 303 K, the unary q_m values for As(V) were 57.40, 52.87, and 81.68 mg g^{-1} for MgO, Mg-Si, and Mg-Si-Zr, respectively, whereas those for F^- were 89.31, 57.38, and 69.31 mg g^{-1}, respectively (Table 1). Thus, Mg-Si-Zr exhibited the highest adsorption capacity for As(V), while MgO retained the strongest intrinsic capacity for F^-. The contrasting responses demonstrate that Si/Zr modification does not simply increase the overall adsorption capacity but alters the relative affinity of the surfaces toward the two anions. The enhanced As(V) capacity of Mg-Si-Zr may partly reflect the contribution of Zr-containing surface groups exhibiting strong affinity toward arsenate through inner-sphere coordination [23], whereas the relatively high F^- capacity retained after Zr incorporation suggests the generation of surface environments favorable for fluoride uptake [49]. These results confirm that compositional modification provides a means of tuning the adsorption preference of Mg-based microspheres.

Temperature-dependent isotherms further revealed that adsorption behavior was strongly dependent on both adsorbate and surface composition. The q_m values for F^- increased from 283 to 303 K for all three adsorbents (Table 1), indicating that fluoride uptake was favored at elevated temperatures and is consistent with an endothermic contribution to the overall adsorption process. In contrast, As(V) adsorption on MgO decreased from 73.89 mg g^{-1} at 283 K to 57.40 mg g^{-1} at 303 K, whereas its q_m increased from 45.11 to 52.87 mg g^{-1} on Mg-Si and from 76.06 to 81.68 mg g^{-1} on Mg-Si-Zr. The reversal from a negative to a positive temperature response following Si/Zr modification suggests incorporation of these elements substantially changes the energetic characteristics of As(V) adsorption, likely through altered surface environments and adsorbate–surface interactions. More broadly, the distinct temperature responses of As(V) adsorption among MgO, Mg-Si, and Mg-Si-Zr indicate that compositional modification substantially alters the thermal response of the adsorption process. However, because q_m is a model-fitted saturation parameter and only two temperatures were investigated (i.e., 283 and 303 K), these trends should not be interpreted as definitive evidence of exothermic or endothermic adsorption. Further thermodynamic investigation would be needed to resolve the underlying contributions. The isotherm results therefore

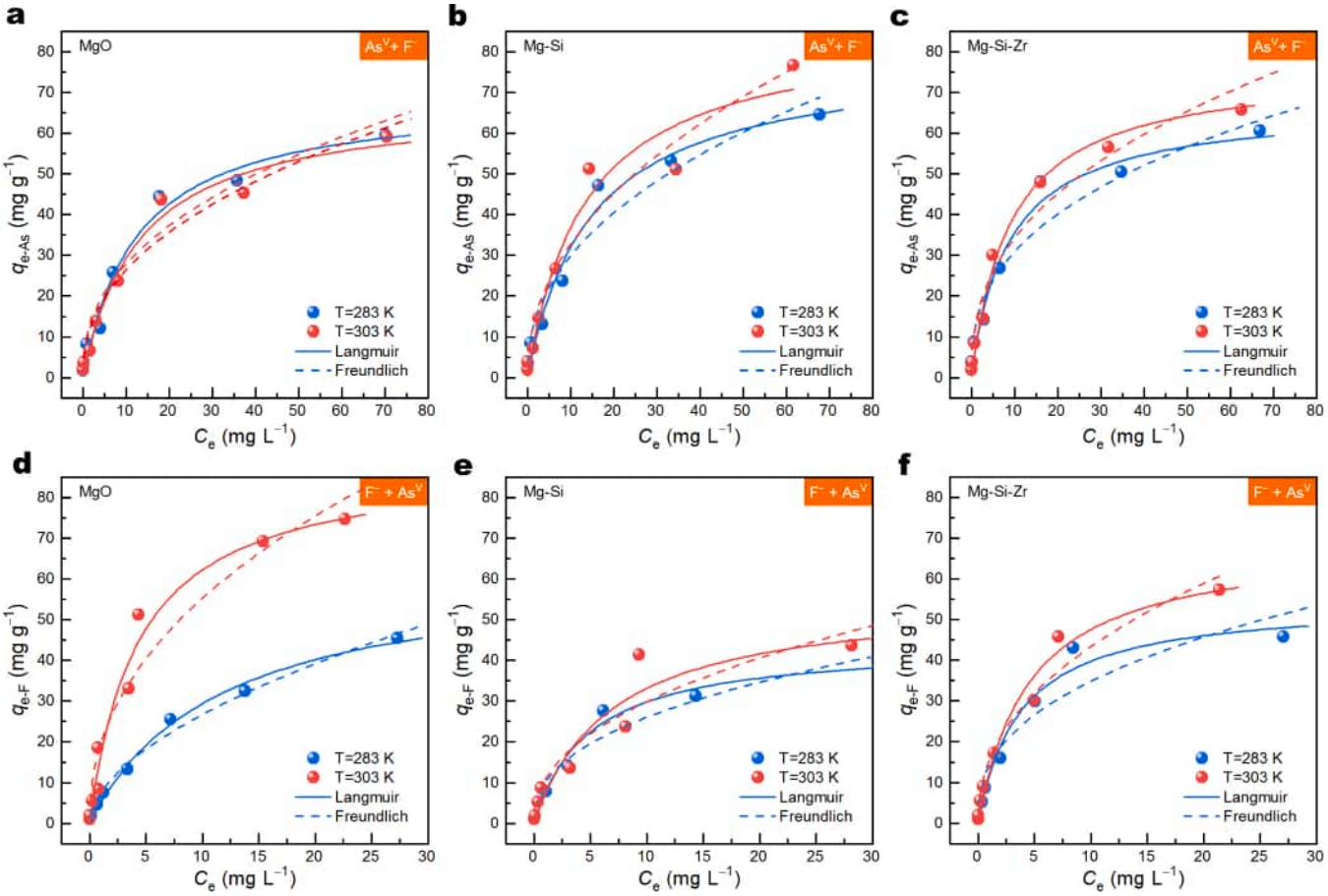


Fig. 6. Adsorption isotherms in binary matrices at 283 and 303 K: (**a**) As(V) on MgO, (**b**) As(V) on Mg-Si, (**c**) As(V) on Mg-Si-Zr, (**d**) F^- on MgO, (**e**) F^- on Mg-Si, and (**f**) F^- on Mg-Si-Zr (ionic strength = 10 mM $NaNO_3$, pH = 7.0, dosage = 0.5 g L^{-1}, contact time = 24 h). Solid and dashed lines represent Langmuir and Freundlich model fits, respectively.

Table 1
Best-fit Langmuir and Freundlich parameters for As(V) and F^- adsorption on these Mg-based microspheres.

Adsorbent	Target adsorbate	Solution	T(K)	Langmuir			Freundlich		
				q_m (mg g^{-1})	k_L	R^2	n	k_F	R^2
MgO	As(V)	As(V)	283	73.89	8.899	0.958	2.165	0.462	0.954
			303	57.40	11.370	0.957	2.703	0.370	0.920
	As(V)	As(V) + F^-	283	69.28	0.419	0.978	5.089	0.419	0.950
			303	67.76	0.432	0.977	2.315	0.432	0.953
	F^-	F^-	283	63.42	0.745	0.992	1.340	0.746	0.989
			303	89.31	19.608	0.974	2.222	0.450	0.944
	F^-	As(V) + F^-	283	62.44	12.702	0.974	5.917	0.448	0.941
			303	84.71	12.198	0.976	1.835	0.545	0.950
Mg-Si	As(V)	As(V)	283	45.11	0.108	0.978	2.732	8.742	0.924
			303	52.87	0.102	0.968	2.564	9.431	0.915
	As(V)	As(V) + F^-	283	37.55	0.172	0.919	2.941	8.750	0.932
			303	49.71	0.076	0.926	2.421	7.474	0.883
	F^-	F^-	283	38.97	0.475	0.994	3.106	13.118	0.941
			303	57.38	0.289	0.993	2.445	14.916	0.977
	F^-	As(V) + F^-	283	44.37	0.204	0.980	2.427	10.075	0.952
			303	55.80	0.146	0.904	2.257	10.773	0.882
Mg-Si-Zr	As(V)	As(V)	283	76.06	0.141	0.980	2.639	12.806	0.949
			303	81.68	0.081	0.976	2.315	12.010	0.974
	As(V)	As(V) + F^-	283	67.50	0.120	0.979	2.653	12.972	0.937
			303	76.07	0.109	0.988	2.479	13.544	0.964
	F^-	F^-	283	54.61	0.267	0.977	2.564	14.205	0.905
			303	69.31	0.218	0.977	2.257	15.625	0.962
	F^-	As(V) + F^-	283	45.07	0.426	0.977	3.155	15.461	0.893
			303	60.11	0.415	0.993	2.745	18.964	0.957

complement the loading-dependent adsorption envelopes in Fig. 4 by demonstrating that structural modification influences not only the number and accessibility of adsorption sites but also their apparent affinity toward As(V) and F^-.

The binary isotherms provide a more stringent evaluation of adsorption performance under coexisting As(V) and F^- conditions (Fig. 6). Compared with unary systems (Fig. 5), the binary adsorption capacities generally decreased, indicating competition for overlapping surface sites. The magnitude of these changes varied with adsorbent composition, demonstrating that Si and Zr incorporation modified not only the overall adsorption capacity but also the competitive behavior toward the two oxyanions. An inhibition ratio, defined as $I = (q_{m,unary} - q_{m,binary})/q_{m,unary} \times 100\%$, was used when binary uptake decreased, whereas an enhancement ratio, $E = (q_{m,binary} - q_{m,unary})/q_{m,unary} \times 100\%$, was used when binary uptake increased (Table S1). On MgO, both species were slightly inhibited at 283 K (I_{As}=6.24%, I_F=1.55%), whereas at 303 K the presence of F^- increased the modeled As(V) capacity by 18.05%, while F^- was inhibited by only 5.15%. Likewise, Mg-Si exhibited similar temperature-dependent interactions, with As(V) inhibited by 16.76% but F^- enhanced by 13.86% at 283 K, while both species showed only modest inhibition at 303 K. These nonuniform responses suggest that As(V)/F^- co-adsorption involves not only competition for overlapping sites but may also reflect changes in the interfacial environment associated with co-adsorption [53,54]. In contrast, Mg-Si-Zr exhibited consistent inhibition of both adsorbates at both temperatures. At 303 K, the As(V) and F^- capacities decreased from 81.68 and 69.31 mg g^{-1} in unary systems to 76.07 and 60.11 mg g^{-1} in the binary system, corresponding to apparent capacity reductions of only 6.87% and 13.27%, respectively (Table S1). Thus, Mg-Si-Zr retained approximately 93% of its unary As(V) capacity and 87% of its F^- capacity under coexisting conditions. Moreover, the consistently higher I_F than I_{As} at both temperatures indicates that F^- uptake was more strongly suppressed by As(V), suggesting a preferential competitive advantage of As(V) on the ternary surface. This behavior may reflect chemically differentiated adsorption environments generated by Si/Zr incorporation, while the specific contribution of Zr-containing sites requires direct spectroscopic evidence. Overall, the isotherm results demonstrate that Mg-Si-Zr combines high As(V) capacity with substantial F^- uptake and comparatively low competitive inhibition, which are also comparable to other Mg-containing adsorbents reported in the literature (Table 2), highlighting its potential for simultaneous removal of these coexisting contaminants. Direct comparison should nevertheless be interpreted cautiously because adsorption capacities and removal rates depend strongly on initial concentration, adsorbent dosage, pH, ionic strength, and test configuration. Although the Mg-based microspheres show promising As(V)/F^- co-removal performance, comprehensive assessment of regeneration, long-term stability, material and energy consumption, and process-scale economics is still required to establish their overall sustainability and practical feasibility. In particular, for practical reuse, an appropriate regeneration strategy should simultaneously promote desorption of As(V) and F^- while minimizing dissolution or structural alteration of the Mg–Si–Zr matrix. Alkaline regeneration represents a potential route for Mg-based adsorbents, but its regeneration efficiency, metal leaching, contaminant recovery, and impact on subsequent adsorption cycles remain to be established for the present Mg-based microspheres [18,55,56].

Table 2
Comparison of maximum adsorption capacity of As(V) and F^- of three Mg-based microspheres with other published data of Mg-containing adsorbents.

Adsorbent	pH	T (K)	Contact time (h)	q_m (mg g^{-1})		Refs
				As(V)	F^-	
Mg/Fe LDH[a]	6.0	298	10	50.24	50.91	[57]
Mg/Fe/La CHLc[b]	6.8	308	10	81.40	73.80	[8]
MgAl-mBC[c]	5.0	283	24	34.45	21.59	[9]
MgO (commercial)	7.0	298	24	8.69	33.10	[10]
Porous MgO	7.0	n/a	n/a	540.90	290.70	[19]
MgLaFe MMO[d]	7.0	298	6	36.96	133.65	[58]
MgLaFe-NS[e]	6.5	303	6	98.70	387.68	[59]
MgO	7.0	303	24	57.40	89.31	this study
Mg-Si	7.0	303	24	52.87	57.38	this study
Mg-Si-Zr	7.0	303	24	81.68	69.31	this study

[a] LDH = layered double hydroxide; [b] CHLc = calcined hydrotalcite-like compound; [c] mBC = magnetic biochar; [d] MMO = mixed metal oxide; [a] NS = nanosheet.

3.5. Spectroscopic evidence and adsorption mechanisms

Given that the above batch adsorption results alone do not constitute definitive evidence for the surface complexation between the Mg-based microspheres and the two adsorbates, the molecular nature of these interactions is therefore examined further using post-adsorption FTIR and XPS analyses. The FTIR spectra provide reliable evidence that surface hydroxyl and metal–oxygen environments participate in the co-uptake of As(V) and F^- by these Mg-based microspheres (Fig. 7a–c). Specifically, for all three adsorbents, the broad O–H stretching band at approximately 3440 cm^{-1} becomes attenuated, broadened, and slightly shifted after adsorption, indicating extensive perturbation of surface hydroxyl groups and their participation in anion uptake [60]. Following As(V) adsorption, a new feature appears at 838–898 cm^{-1} , which is attributable to As–O vibrations of surface-associated arsenate species [60]. The emergence of this feature for MgO, Mg-Si, and Mg-Si-Zr indicates that As(V) interacts directly with the hydroxylated metal–oxygen surfaces rather than being retained solely through nonspecific electrostatic attraction [61]. Meanwhile, the changes in the 400–600 cm^{-1} region, particularly around 522–550 cm^{-1} , indicate perturbation of

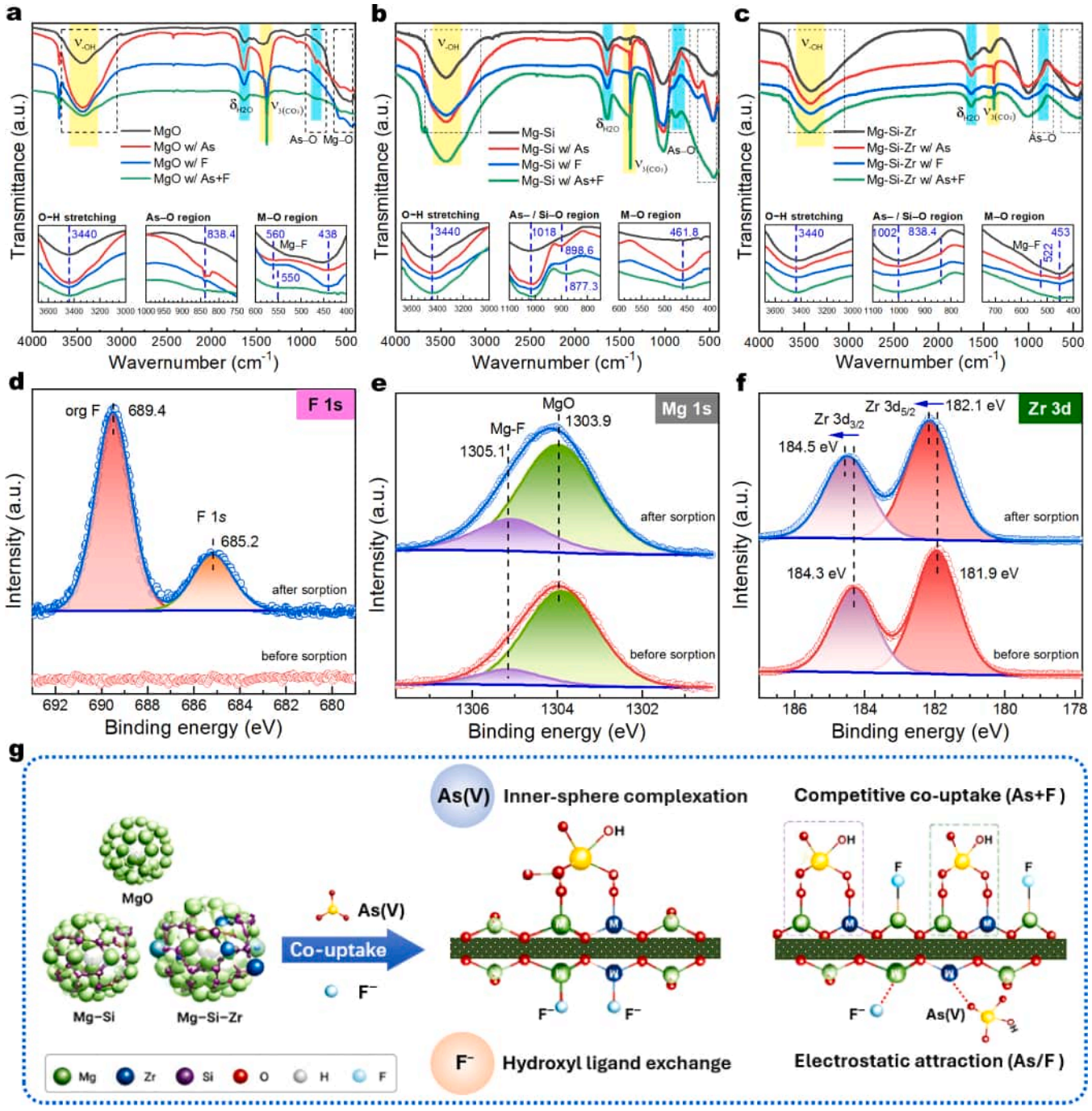


Fig. 7. Spectroscopic evidence and proposed mechanism for the co-uptake of As(V) and F^- by Mg-based microspheres. (**a**–**c**) FTIR spectra of MgO, Mg-Si, and Mg-Si-Zr before and after adsorption of As(V), F^-, and As(V) + F^-, highlighting changes in surface hydroxyl, metal–oxygen, and adsorbate-related vibrational bands. (**d**–**f**) High-resolution XPS spectra of (**d**) F 1 s, (**e**) Mg 1 s, and (**f**) Zr 3d regions before and after binary adsorption. (**g**) Schematic illustration of the proposed As(V)/F^- co-uptake mechanism, involving surface hydroxyl-mediated ligand exchange, inner-sphere complexation, electrostatic attraction, and competitive occupation of adsorption sites (Note that the three Mg-based microspheres in panel **g** don't represent a detailed molecular or morphological model).

Mg–O/Zr–O coordination environments following adsorption [62]. Collectively, the attenuation of surface –OH groups, formation of As–O species, and perturbation of metal–oxygen vibrations support a hydroxyl-mediated ligand-exchange pathway involving specific surface complexation of As(V) [60,61].

The XPS results for Mg-Si-Zr after binary adsorption further demonstrate the involvement of Mg-, Zr-, and O-associated surface environments in As(V)/F^- co-uptake (Fig. 7d–f and S3). For instance, the appearance of a dominant F 1 s contribution at approximately 685.2 eV is consistent with surface-associated metal fluoride interactions, while the sharp feature near 689.4 eV may reflect a more polarized or localized organic fluoride contaminant [62]. The increased contribution at approximately 1305.1 eV in the Mg 1 s spectrum after adsorption indicates a modified electronic environment around Mg sites following interaction with the anionic adsorbates (Fig. 7e). In addition, a + 0.2 eV positive shift in the Zr 3d region indicates altered electronic density around Zr following As(V)/F^- uptake (Fig. 7f), and is consistent with its participation in specific interactions with the adsorbed anions [23,62]. The O 1 s hydroxyl-related component also shifts from approximately 531.6–531.8 eV, corroborating modification of surface oxygen/-hydroxyl environments during adsorption [62]. Notably, no distinct As 3d signal could be reliably identified in the XPS spectrum of the Mg–Si–Zr microspheres after binary adsorption (Fig. 7d–f and S3). Reinspection of the spectrum revealed a strong feature at approximately 39.0–39.5 eV within the As 3d analytical region (possibly assigned to Tc 4p/Tm 5p), which complicates background definition and the identification of a weak As 3d contribution (Fig. S3d). In addition, XPS is intrinsically surface-sensitive, and its detection limit depends strongly on the spectral background and matrix composition [63–65]. Therefore, the absence of a resolvable As 3d signal should not be interpreted as evidence that As was not retained by the adsorbent. It may reflect a low or spatially heterogeneous surface concentration of adsorbed As and/or attenuation of the As signal by the surrounding Mg–Si–Zr matrix. The As–O vibration observed by FTIR after adsorption (Fig. 7a–c), together with the changes in the O 1 s, Mg 1 s, and Zr 3d environments, provides complementary evidence for interaction of As(V) with hydroxylated Mg/Zr surface domains [64]. Nevertheless, because the As 3d signal was not independently resolved by XPS, the present data do not permit definitive identification of a unique As surface species or exclusion of other As-bearing configurations. In addition, MgO often has a positively charged surface in solution due to its high isoelectric point [7], which undoubtedly attracts two anions via electrostatic force. Therefore, electrostatic attraction cannot be excluded from these interactions. Collectively, FTIR and XPS results support a mechanism involving surface hydroxyl-mediated ligand exchange and specific surface complexation of As(V) and F^- at Mg- and Zr-associated sites, consistent with surface-associated fluoride and altered Mg/Zr coordination environments [21,23]. Nevertheless, the ex-situ XPS shifts should be interpreted collectively rather than as definitive proof of individual Mg–F, Zr–F, or Zr–O–As bonds because binding-energy changes alone cannot uniquely resolve local coordination geometries.

Integrating the spectroscopic results with the adsorption envelopes suggests a plausibly dual but partially overlapping co-adsorption mechanism, along with the ubiquitous electrostatic attraction (Fig. 7g). As(V) uptake is primarily attributed to hydroxyl-mediated ligand exchange and formation of inner-sphere As–O surface complexes [9,23], whereas F^- interacts specifically with Mg- and/or Zr-associated sites, plausibly through ligand exchange, formation of metal-associated fluoride species, and electrostatic attraction [66]. These specific interactions explain the strong adsorption observed over a broad pH range and the relatively weak influence of ionic strength, particularly for As(V) [23]. At the same time, the modest capacity reductions observed in binary systems indicate partial competition for overlapping adsorption domains, while the incomplete inhibition demonstrates the presence of chemically differentiated surface sites s [43,44]. Accordingly, the Mg-Si-Zr microspheres can be regarded as heterogeneous interfaces comprising Mg-associated, Si-modified, and Zr-associated environments that provide complementary binding sites for the two anions. Overall, the spectroscopic evidence is consistent with the possible participation of hydroxyl-mediated ligand exchange and specific surface complexation, coupled with partial competition between As(V) and F^- for shared surface sites, thereby enabling substantial simultaneous uptake of both contaminants (see Eqs. (5–8), M = Mg, Zr). However, because the analyses were conducted ex situ and the observed spectral changes do not uniquely identify molecular coordination structures, the relative contributions of inner-sphere complexation, electrostatic interactions, and other surface-association processes cannot be conclusively resolved. The proposed mechanism should therefore be regarded as a plausible interpretation of the available evidence rather than a definitive assignment of specific surface complexes.

$$\equiv M-OH + HAsO_4^{2-} \rightarrow \equiv M-O-As(V) + OH^- \quad (5)$$

$$\equiv M-OH_2^+ + HAsO_4^{2-} \rightarrow \equiv M-OH_2^+\cdots As(V) \quad (6)$$

$$\equiv M-OH + F^- \rightarrow \equiv M-F + OH^- \quad (7)$$

$$\equiv M-OH_2^+ + F^- \rightarrow \equiv M-OH_2^+\cdots F^- \quad (8)$$

4. Conclusions

This study demonstrated that compositional engineering of Mg-based microspheres provides an effective strategy for regulating the co-uptake of As(V) and F^- from aqueous systems. Incorporation of Si greatly altered the physicochemical characteristics of MgO and enhanced As(V) uptake, while further introduction of Zr created complementary microenvironments that improved the overall balance between As(V) and F^- removal. All three microspheres exhibited a pronounced decrease in removal under strongly acidic conditions, likely associated with acid-induced alteration of the Mg-containing surface/matrix, but maintained relatively stable adsorption from pH 5.0–11.0. The limited influence of ionic strength, particularly on As(V) uptake, together with the progressive decrease in fractional removal at increasing surface loading, indicates that adsorption was dominated by specific interactions at heterogeneous surface sites rather than nonspecific electrostatic accumulation. The equilibrium results further demonstrated distinct adsorption preferences among the materials. MgO showed the highest F^- capacity, whereas Si modification enhanced As(V) uptake, and Mg–Si–Zr exhibited the most favorable overall dual-contaminant performance, achieving Langmuir capacities of 81.68 mg g^{-1} for As(V) and 69.31 mg g^{-1} for F^- at 303 K in unary systems. Despite competition in the binary matrix, Mg–Si–Zr retained large capacities of 76.07 and 60.11 mg g^{-1} for As(V) and F^-, respectively, indicating that the two anions compete only partially for surface sites. Spectroscopic analyses further revealed perturbation of surface hydroxyl and metal–oxygen environments, formation of surface-associated As–O species, emergence of metal-associated fluoride, and changes in Mg/Zr electronic environments. Collectively, these findings support a co-uptake mechanism dominated by hydroxyl-mediated ligand exchange and specific inner-sphere complexation at Mg- and Zr-associated sites, accompanied by limited contribution from electrostatic attraction and partial competition between As(V) and F^- for overlapping adsorption sites. Nevertheless, several limitations should be acknowledged. The ex-situ FTIR and XPS results support the proposed adsorption mechanisms but cannot unambiguously resolve the molecular configurations of the surface complexes. In addition, the experiments were conducted under controlled batch conditions and did not fully account for the complexity of natural water matrices or long-term regeneration and stability. A further limitation is that the Si and Zr contents were not systematically varied. Consequently, the selected formulations represent comparative compositions rather than optimized materials, and further composition-

screening studies are needed. Future work should therefore combine molecular-scale in-situ characterization with realistic multicomponent waters and continuous-flow/regeneration tests to further validate the practical applicability of Mg–Si–Zr microspheres.

CRediT authorship contribution statement

Zhao Hu: Writing – original draft, Investigation. **Xianfei Wang:** Investigation, Validation. **Jingjing Fu:** Investigation, Validation. **Jiantao Xu:** Validation, Formal analysis. **Feihu Li:** Writing – review & editing, Visualization, Supervision, Conceptualization.

Declaration of Competing Interest

The authors declare that they have no known competing financial interests or personal relationships that could have appeared to influence the work reported in this paper.

Acknowledgments

The work was partially supported by the Priority Academic Program Development (PAPD) of Jiangsu Higher Education Institutions, and the National Natural Science Foundation of China (51002080, 41501197).

Appendix A. Supporting information

Supplementary data associated with this article can be found in the online version at doi:10.1016/j.jece.2026.125606.

Data availability

Data will be made available on request.

References

[1] Z. Wang, H.M. Guo, N. Adimalla, J.L. Pei, Z. Zhang, H.Y. Liu, Co-occurrence of arsenic and fluoride in groundwater of Guide basin in China: genesis, mobility and enrichment mechanism, Environ. Res. 244 (2024) 117920, https://doi.org/10.1016/j.envres.2023.117920.

[2] H.N. Goodwin, T. Roh, R. Buskirk, D.K. Nordstrom, F. Marcantonio, P.S. K. Knappett, Hydrogeochemical processes driving elevated arsenic and fluoride in the Texas Gulf Coast aquifer, Appl. Geochem. 200 (2026) 106713, https://doi.org/10.1016/j.apgeochem.2026.106713.

[3] Y.Q. Zhang, R.Y. Huang, Z.J. Gao, Y.R. Niu, Driving forces and health risks of fluoride and arsenic in geothermal water: insights from hydrogeochemical analysis, deterministic and Monte Carlo models, Environ. Geochem. Health 48 (3) (2026) 149, https://doi.org/10.1007/s10653-026-03049-3.

[4] Y.N. Yan, J.W. Zhang, N. Wu, Z.H. Xia, L. Liu, Z.Q. Zhao, Co-occurrence of elevated arsenic and fluoride concentrations in Wuliangsu Lake: implications for the genesis of poor-quality groundwater in the (paleo-)Huanghe (Yellow River) catchment, China, Water Res. 258 (2024) 121767, https://doi.org/10.1016/j.watres.2024.121767.

[5] N.Z. Xu, L. Liu, M.J. Tan, X.H. Tao, L. Li, H.S. Wang, J.S. Gong, Co-occurrence, sources and co-enrichment mechanism of arsenic, fluoride in groundwater from Huaihe River Basin, China, Emerg. Contam. 10 (1) (2024) 100276, https://doi.org/10.1016/j.emcon.2023.100276.

[6] H.X. Liu, X.J. Xie, Y.X. Wang, Selective arsenic removal in complex aquatic environments: mechanistic insights, sorbent design, and environmental regulation, J. Hazard. Mater. 501 (2026) 140761, https://doi.org/10.1016/j.jhazmat.2025.140761.

[7] Z. Jin, Y. Jia, K.S. Zhang, L.T. Kong, B. Sun, W. Shen, F.L. Meng, J.H. Liu, Effective removal of fluoride by porous MgO nanoplates and its adsorption mechanism, J. Alloy. Compd. 675 (2016) 292–300, https://doi.org/10.1016/j.jallcom.2016.03.118.

[8] P. Wu, L. Xia, Y. Liu, J.S. Wu, Q.Y. Chen, S.X. Song, Simultaneous sorption of arsenate and fluoride on calcined Mg-Fe-La hydrotalcite-like compound from water, ACS Sustain. Chem. Eng. 6 (12) (2018) 16287–16297, https://doi.org/10.1021/acssuschemeng.8b03209.

[9] Z.Y. Shen, J. Jin, J.J. Fu, M. Yang, F.H. Li, Anchoring Al- and/or Mg-oxides to magnetic biochars for Co-uptake of arsenate and fluoride from water, J. Environ. Manag. 293 (2021) 112898, https://doi.org/10.1016/j.jenvman.2021.112898.

[10] H. Sugita, K. Morimoto, T. Saito, J. Hara, Simultaneous removal of arsenate and fluoride using magnesium-based adsorbents, Sustainability 16 (5) (2024) 1774, https://doi.org/10.3390/su16051774.

[11] X.Y. Sun, C.P. Ke, Q.F. Lu, Q. Wang, S.Q. Zhou, L. Liang, G.Y. Xie, Recent advances in adsorption techniques for the removal of fluoride ions from wastewater: a review, Ind. Eng. Chem. Res. 63 (46) (2024) 19936–19954, https://doi.org/10.1021/acs.iecr.4c02734.

[12] F.H. Li, J.J. Fu, J. Jin, S.L. Wang, Y.Y. Liu, M. Yang, X.R. Fu, Evaporation-induced self-assembly (EISA) synthesized mesoporous bimetallic oxides (MBOs) enabling enhanced co-uptake of arsenate and fluoride from water, J. Chem. Technol. Biotechnol. 94 (3) (2019) 879–891, https://doi.org/10.1002/jctb.5835.

[13] A. Acharya, G. Jeppu, C.R. Girish, B. Prabhu, V.R. Murty, A.S. Martis, S. Ramesh, Adsorption of arsenic and fluoride: modeling of single and competitive adsorption systems, Heliyon 10 (11) (2024) e31967, https://doi.org/10.1016/j.heliyon.2024.e31967.

[14] A. Acharya, L.N. Disha, Y. Puri, S.M. Kini, G. Jeppu, C.R. Girish, Competitive adsorption of arsenic(V) and fluoride in packed-bed column: experimental and modeling studies, Appl. Water Sci. 15 (10) (2025) 264, https://doi.org/10.1007/s13201-025-02610-2.

[15] J. Liu, B. Wang, M. Chen, P. Wu, M. Hassan, X.Y. Zhang, Synergistic removal of arsenic and fluoride dual contaminants in water by engineered phosphogypsum-biochar composite: Adsorption behavior and mechanisms, J. Environ. Chem. Eng. 13 (5) (2025) 118316, https://doi.org/10.1016/j.jece.2025.118316.

[16] F.J. Xiao, G.B. Jiang, D. Bu, J.J. Fu, X.M. Cui, Q.Y. Zhang, Rapid and synergistic adsorption of arsenic and fluoride by bifunctional Al/ Ce oxides in complex geothermal matrices, Ecotoxicol. Environ. Saf. 306 (2025) 119362, https://doi.org/10.1016/j.ecoenv.2025.119362.

[17] E. Alemu, A. Mandpe, S. More, D. Beyene, E. Alemayehu, Simultaneous removal of fluoride and arsenic from water in a fixed-bed column using Fe-Al-MOF/CF composite: optimization by response surface methodology, Sci. Rep. 16 (2026) 23343, https://doi.org/10.1038/s41598-026-53387-6.

[18] L. Shi, S.L. Zhao, X.X. Wang, J.L. He, Y. Zhao, K.Z. Wang, Layered magnesium oxide for efficient removal of fluoride from groundwater, New. J. Chem. 49 (8) (2025) 3293–3304, https://doi.org/10.1039/d4nj05145a.

[19] P.P. Gao, X.K. Tian, C. Yang, Z.X. Zhou, Y. Li, Y.X. Wang, S. Komarneni, Fabrication, performance and mechanism of MgO meso-/macroporous nanostructures for simultaneous removal of As(III) and F in a groundwater system, Environ. Sci. -Nano 3 (6) (2016) 1416–1424, https://doi.org/10.1039/c6en00400h.

[20] W. Li, D.H. Chen, F. Xia, J.Z.Y. Tan, P.P. Huang, W.G. Song, N.M. Nursam, R. A. Caruso, Extremely high arsenic removal capacity for mesoporous aluminium magnesium oxide composites, Environ. Sci. -Nano 3 (1) (2016) 94–106, https://doi.org/10.1039/c5en00171d.

[21] X.P. Cao, Y.D. Zhong, H. Zhang, H. Zhao, C. Meng, L.L. Zhou, R.J. Liu, Deep removal of fluoride by highly activated magnesium oxide, ACS ES&T Water 4 (6) (2024) 2756–2763, https://doi.org/10.1021/acsestwater.4c00403.

[22] L.T. Zhang, C.Y. Cui, C.M. Zhu, L. Gong, M. Li, S.W. Xiang, B. Yu, High-efficiency fluoride removal using hierarchical flower-like magnesium oxide: adsorption characteristics and mechanistic insights, New. J. Chem. 48 (39) (2024) 17268–17276, https://doi.org/10.1039/d4nj03012e.

[23] P. Shen, S. Pan, X. Huang, X. Zhang, Nanoconfinement boosts affinity of hydrated zirconium oxides to arsenate: surface complexation modeling study, Chemosphere 349 (2024) 140912, https://doi.org/10.1016/j.chemosphere.2023.140912.

[24] H.N. Mo, H.M. Shan, H.B. Zhan, H.M. Liao, B. An, S.X. Peng, Selective and competitive adsorption of arsenite and fluoride by ternary Fe-Zr-Al oxide composites: insights into multi-component removal mechanisms, Colloids Surf. A 737 (2026) 139944, https://doi.org/10.1016/j.colsurfa.2026.139944.

[25] H.W. Myers, B.C. Ma, X.F. Wang, D.W. Li, F.H. Li, Magnetic chitosan-based biosorbents for phosphorus removal from wastewater: adsorption properties and mechanistic insights, Int. J. Biol. Macromol. 347 (2026) 150609, https://doi.org/10.1016/j.ijbiomac.2026.150609.

[26] L. Kuai, J. Geng, C.Y. Chen, E.J. Kan, Y.D. Liu, Q. Wang, B.Y. Geng, A reliable aerosol-spray-assisted approach to produce and optimize amorphous metal oxide catalysts for electrochemical water splitting, Angew. Chem. Int. Ed. 53 (29) (2014) 7547–7551, https://doi.org/10.1002/anie.201404208.

[27] C.K. Tsung, J. Fan, N.F. Zheng, Q.H. Shi, A.J. Forman, J.F. Wang, G.D. Stucky, A general route to diverse mesoporous metal oxide submicrospheres with highly crystalline frameworks, Angew. Chem. Int. Ed. 47 (45) (2008) 8682–8686, https://doi.org/10.1002/anie.200802487.

[28] C.J. Lin, Y.H. Liou, Y.C. Zhang, C.L. Chen, C.L. Dong, S.Y. Chen, G.D. Stucky, Mesoporous Fe-doped TiO_2 sub-microspheres with enhanced photocatalytic activity under visible light illumination, Appl. Catal. B Environ. 127 (2012) 175–181, https://doi.org/10.1016/j.apcatb.2012.08.011.

[29] F.H. Li, J. Jin, Z.Y. Shen, H.S. Ji, M. Yang, Y.M. Yin, Removal and recovery of phosphate and fluoride from water with reusable mesoporous Fe_3O_4@*m*SiO_2@*m*LDH composites as sorbents, J. Hazard. Mater. 388 (2020) 121734, https://doi.org/10.1016/j.jhazmat.2019.121734.

[30] J.B. Shi, Z.Y. Tang, Z.X. Jin, Q. Chi, B. He, G.B. Jiang, Determination of As(III) and As(V) in soils using sequential extraction combined with flow injection hydride generation atomic fluorescence detection, Anal. Chim. Acta 477 (1) (2003) 139–147, https://doi.org/10.1016/S0003-2670(02)01402-2.

[31] F.H. Li, H. Fu, J.P. Zhai, Q. Li, Synthesis of mesostructured ferric oxyhydroxides templated by alkyl surfactants: effect of pH, F^- and solvents, and their adsorption isotherms for As(V), Microporous Mesoporous Mater. 123 (1-3) (2009) 177–184, https://doi.org/10.1016/j.micromeso.2009.03.044.

[32] V.V. Revin, A.V. Dolganov, E.V. Liyaskina, N.B. Nazarova, A.V. Balandina, A. A. Devyataeva, V.D. Revin, Characterizing bacterial cellulose produced by komagataeibacter sucrofermentans H-110 on molasses medium and obtaining a

biocomposite based on it for the adsorption of fluoride, Polymers 13 (9) (2021) 1422, https://doi.org/10.3390/polym13091422.
[33] Y. Boyjoo, M.W. Wang, V.K. Pareek, J. Liu, M. Jaroniec, Synthesis and applications of porous non-silica metal oxide submicrospheres, Chem. Soc. Rev. 45 (21) (2016) 6013–6047, https://doi.org/10.1039/c6cs00060f.
[34] Y. Liu, Q. Li, S.A. Gao, J.K. Shang, Exceptional As(III) sorption capacity by highly porous magnesium oxide nanoflakes made from hydrothermal synthesis, J. Am. Ceram. Soc. 94 (1) (2011) 118–124, https://doi.org/10.1111/j.1551-2916.2010.04043.x.
[35] M. Saraiva, V. Georgieva, S. Mahieu, K. Van Aeken, A. Bogaerts, D. Depla, Compositional effects on the growth of Mg(M)O films, J. Appl. Phys. 107 (3) (2010) 034902, https://doi.org/10.1063/1.3284949.
[36] F.H. Li, W.H. Wu, R.Y. Li, X.R. Fu, Adsorption of phosphate by acid-modified fly ash and palygorskite in aqueous solution: experimental and modeling, Appl. Clay Sci. 132 (2016) 343–352, https://doi.org/10.1016/j.clay.2016.06.028.
[37] A.T. Bah, Z.Y. Shen, J.N. Yan, F.H. Li, Phosphorous recovery from water via batch adsorption enrichment combined with struvite crystallization in a fluidized bed reactor, J. Environ. Chem. Eng. 11 (3) (2023) 110180, https://doi.org/10.1016/j.jece.2023.110180.
[38] F.H. Li, Layer-by-layer loading iron onto mesoporous silica surfaces: synthesis, characterization and application for As(V) removal, Microporous Mesoporous Mater. 171 (2013) 139–146, https://doi.org/10.1016/j.micromeso.2012.12.025.
[39] V.Q. Chiu, J.G. Hering, Arsenic adsorption and oxidation at manganite surfaces. 1. Method for simultaneous determination of adsorbed and dissolved arsenic species, Environ. Sci. Technol. 34 (10) (2000) 2029–2034, https://doi.org/10.1021/Es990788p.
[40] M. Zelenka, E.H.G. Backus, MgO-water interface: structure and surface dissolution depend on flow and pH, Phys. Chem. Chem. Phys. 27 (43) (2025) 23356–23364, https://doi.org/10.1039/d5cp03295d.
[41] S. Mehanathan, J. Jaafar, A.M. Nasir, A.F. Ismail, T. Matsuura, M.H.D. Othman, M. A. Rahman, N. Yusof, Magnesium oxide nanoparticles for the adsorption of pentavalent arsenic from water: effects of calcination, Membranes 13 (5) (2023) 475, https://doi.org/10.3390/membranes13050475.
[42] K.S. Zhang, S.B. Wu, X.L. Wang, J.Y. He, B. Sun, Y. Jia, T. Luo, F.L. Meng, Z. Jin, D. Y. Lin, W. Shen, L.T. Kong, J.H. Liu, Wide pH range for fluoride removal from water by MHS-MgO/$MgCO_3$ adsorbent: kinetic, thermodynamic and mechanism studies, J. Colloid Interface Sci. 446 (2015) 194–202, https://doi.org/10.1016/j.jcis.2015.01.049.
[43] M. Channegowda, Recent advances in environmentally benign hierarchical inorganic nano-adsorbents for the removal of poisonous metal ions in water: a review with mechanistic insight into toxicity and adsorption, Nanoscale Adv. 2 (12) (2020) 5529–5554, https://doi.org/10.1039/d0na00650e.
[44] G.S. Zhang, Z.J. Wu, Q.Y. Qiu, Y.Q. Wang, Efficient sorption of arsenic on nanostructured Fe-Cu binary oxides: influence of structure and crystallinity, Front. Chem. 9 (2022) 840446, https://doi.org/10.3389/fchem.2021.840446.
[45] G.T. Tee, X.Y. Gok, W.F. Yong, Adsorption of pollutants in wastewater via biosorbents, nanoparticles and magnetic biosorbents: a review, Environ. Res. 212 (2022) 113248, https://doi.org/10.1016/j.envres.2022.113248.
[46] J.Z. Di, Z. Ruan, S.Y. Zhang, Y.R. Dong, S.O. Fu, H.Z. Li, G.L. Jiang, Adsorption behaviors and mechanisms of Cu^{2+}, Zn^{2+} and Pb^{2+} by magnetically modified lignite, Sci. Rep. 12 (2022) 1394, https://doi.org/10.1038/s41598-022-05453-y.
[47] F. Sevim, O. Laçin, F. Demir, O.F. Erkiliç, Adsorption capacity, isotherm, kinetics, and thermodynamics examinations on the removal of a textile azo dye by local natural adsorbent, Glob. Chall. 9 (5) (2025) 2500024, https://doi.org/10.1002/gch2.202500024.
[48] X.Y. Xia, S. Litvinov, M. Muhler, Consistent approach to adsorption thermodynamics on heterogeneous surfaces using different empirical energy distribution models, Langmuir 22 (19) (2006) 8063–8070, https://doi.org/10.1021/la061233s.
[49] L.H. Velazquez-Jimenez, R.H. Hurt, J. Matos, J.R. Rangel-Mendez, Zirconium-carbon hybrid sorbent for removal of fluoride from water: oxalic acid mediated Zr (IV) assembly and adsorption mechanism, Environ. Sci. Technol. 48 (2) (2014) 1166–1174, https://doi.org/10.1021/es403929b.
[50] H. Freundlich, Über die adsorption in Lösungen, Z. Phys. Chem. 57 (1907) 385–470.
[51] I. Langmuir, The adsorption of gases on plane surfaces of glass, mica and platinum, J. Am. Chem. Soc. 40 (1918) 1361–1403, https://doi.org/10.1021/ja02242a004.
[52] K.Y. Foo, B.H. Hameed, Insights into the modeling of adsorption isotherm systems, Chem. Eng. J. 156 (1) (2010) 2–10, https://doi.org/10.1016/j.cej.2009.09.013.
[53] R.P. Liu, W.X. Gong, H.C. Lan, T.M. Yang, H.J. Liu, J.H. Qu, Simultaneous removal of arsenate and fluoride by iron and aluminum binary oxide: competitive adsorption effects, Sep. Purif. Technol. 92 (2012) 100–105, https://doi.org/10.1016/j.seppur.2012.03.020.
[54] K. Wu, N. Zhang, T. Liu, C. Ma, P.K. Jin, F.R. Zhang, J. Zhang, X.C. Wang, Competitive adsorption behaviors of arsenite and fluoride onto manganese-aluminum binary adsorbents, Colloids Surf. A 529 (2017) 185–194, https://doi.org/10.1016/j.colsurfa.2017.05.039.
[55] S. Tresintsi, K. Simeonidis, M. Katsikini, E.C. Paloura, G. Bantsis, M. Mitrakas, A novel approach for arsenic adsorbents regeneration using MgO, J. Hazard. Mater. 265 (2014) 217–225, https://doi.org/10.1016/j.jhazmat.2013.12.003.
[56] Q. Zhou, B. Ren, Y. Wei, S. Tian, X. Jin, F. Jiang, Z. Lin, X. Yang, Efficient removal of fluoride from water: adsorption performance of MgO-x adsorbents derived from Mg-MOF-74 and insights from DFT calculations, Sep. Purif. Technol. 352 (2025) 128190, https://doi.org/10.1016/j.seppur.2024.128190.
[57] D.J. Kang, X.L. Yu, S.R. Tong, M.F. Ge, J.C. Zuo, C.Y. Cao, W.G. Song, Performance and mechanism of Mg/Fe layered double hydroxides for fluoride and arsenate removal from aqueous solution, Chem. Eng. J. 228 (2013) 731–740, https://doi.org/10.1016/j.cej.2013.05.041.
[58] X. Wang, J. Zhu, W. Li, H. Wang, Synthesis of MgLaFe MMO composites and their adsorption properties for Co-removal of fluoride and arsenic from water, Acad. J. Sci. Technol. 9 (1) (2024) 96–100, https://doi.org/10.54097/aayvry68.
[59] X.T. Wang, J.F. Zhu, L. Qi, Y.H. Qin, B.P. Ren, X.J. Wang, Co-sorption of arsenic and fluoride using the hierarchical Mg-La-Fe nanosheets derived from layered double oxides, Chem. Eng. J. 499 (2024) 156340, https://doi.org/10.1016/j.cej.2024.156340.
[60] S. Goldberg, C.T. Johnston, Mechanisms of arsenic adsorption on amorphous oxides evaluated using macroscopic measurements, vibrational spectroscopy, and surface complexation modeling, J. Colloid Interf. Sci. 234 (1) (2001) 204–216, https://doi.org/10.1006/jcis.2000.7295.
[61] K. Fukushi, D.A. Sverjensky, A predictive model (ETLM) for arsenate adsorption and surface speciation on oxides consistent with spectroscopic and theoretical molecular evidence, Geochim. Cosmochim. Acta 71 (15) (2007) 3717–3745, https://doi.org/10.1016/j.gca.2007.05.018.
[62] X.M. Dou, D. Mohan, C.U. Pittman, S. Yang, Remediating fluoride from water using hydrous zirconium oxide, Chem. Eng. J. 198-199 (2012) 236–245, https://doi.org/10.1016/j.cej.2012.05.084.
[63] Y.S. Kang, D.K. Kim, K.S. Jeong, M.H. Cho, C.Y. Kim, K.B. Chung, H. Kim, D.C. Kim, Structural evolution and the control of defects in atomic layer deposited HfO_2-Al_2O_3 stacked films on GaAs, ACS Appl. Mater. Interfaces 5 (6) (2013) 1982–1989, https://doi.org/10.1021/am302803f.
[64] P.Y. Wu, Y.P. Jiang, Q.Y. Zhang, Y. Jia, D.Y. Peng, W. Xu, Comparative study on arsenate removal mechanism of MgO and MgO/TiO_2 composites: FTIR and XPS analysis, New. J. Chem. 40 (3) (2016) 2878–2885, https://doi.org/10.1039/c5nj02358k.
[65] F.H. Li, M. Y. Ma, Magnetic Biocomposites for wastewater remediation, in R. Bouhfid, N. Zari, A. Qaiss (Eds.), Biocomposite Materials for Wastewater Remediation, John Wiley & Sons, Inc., Hoboken, New Jersey, 2026, pp. 287 - 318, 10.1002/9781394246489.ch10.
[66] L.X. Li, D. Xu, X.Q. Li, W.C. Liu, Y. Jia, Excellent fluoride removal properties of porous hollow MgO microspheres, New. J. Chem. 38 (11) (2014) 5445–5452, https://doi.org/10.1039/c4nj01361a.